Dynamics of dynein at microtubule plus-ends and the cortex during the division of the *C. elegans* zygote

Ruddi Rodriguez Garcia[1,2,3,*], Laurent Chesneau[1,2,*], Sylvain Pastezeur[1,2], Julien Roul[1,2,4], Marc Tramier[1,2] and Jacques Pécréaux[1,2,#]

1. CNRS, UMR6290, F-35043 Rennes, France

2. University Rennes 1, UEB, SFR Biosit, School of medicine, F-35043 Rennes, France

3. Present address: Cell Biology, Faculty of Science, Utrecht University, Padualaan 8, 3584 CH Utrecht, The Netherlands.

4. Present address: LAAS - Laboratoire d'analyse et d'architecture des systèmes, 7, avenue du Colonel Roche BP 54200, 31031 Toulouse cedex 4, France.

* These authors contributed equally

Corresponding author: Jacques Pécréaux

CNRS UMR6290 - 2 avenue du Prof. Léon Bernard - 35043 Rennes - France

email: jacques.pecreaux@univ-rennes1.fr

Running title: Dynamics of dynein in the *C. elegans* zygote

Abstract

During asymmetric cell divisions, cortical dyneins generate forces essential to position the spindle after polarity cues, prescribing daughter cells fate. In nematode zygote, cortical dynein pulls on microtubules transiently, raising the question of its targeting and dynamics. Tracking and fluorescence correlation spectroscopy revealed that in the cytoplasm, dynein spots displayed directed motions toward the cortex, localized at microtubule plus-ends through EBP-2/EB but are not actively transported. Surprisingly CLIP-1/CLIP170 is not involved. *ebp-2(0)* slightly reduced spindle rocking, thus most cortical forces remain suggesting a redundant mechanism.

At the cortex, to relate dynein residency and forces generating, we tracked dynein and found two dynamically distinct populations. One of them would correspond to force generating events. Our experiments also indicated that an asymmetric (polarized) dynein–microbutule on-rate, causes the force imbalance positioning the spindle. GPR-1/2 increases the overall dynein density but also residency time (pulling processivity), although this latter was not polarized.

Introduction

Successful symmetric and asymmetric cell divisions rely on precise positioning and orientation of the mitotic spindle, ensuring a correct partitioning of chromosomes and cell organelles. The microtubule molecular motor dynein is key to generate the required forces[1, 2, 3, 4, 5, 6, 7, 8, 9, 10, 11]. From yeast to human, dynein is localized at the cell cortex and generates pulling forces on astral microtubules emanating from the spindle poles[12]. Cytoplasmic dynein (hereafter referred to as dynein) is minus-end directed, i.e. running towards spindle pole bodies (SPB)/centrosomes. It is involved in numerous functions among which spindle assembly checkpoint and spindle positioning during mitosis but also retrograde vesicular traffic in interphase cells and neuronal axons e.g.[13]. Dynein is a dimer of a multi-subunit complex fulfilling various functions specified by the involved subunits[14]. They are well conserved through evolution and include: heavy chain (HC), intermediate chain (IC), light intermediate chain (LIC) and light chain (LC)[15]. The HCs, which are members of the AAA ATPase protein superfamily, are the force-producing components[16]. In vertebrates, various ICs ensure cargo binding specificity[14]. In contrast, in *C. elegans*, a single homolog of IC exists, DYCI-1, and its depletion phenocopies mostly the loss of heavy chain[17, 18].

In many organisms including mammalian cells[19, 20], dynein decorates microtubule ends distal from spindle poles, termed plus-ends. However, it is unclear whether it is transported towards the cell periphery and whether such a process has a relevance to cell division in metazoans. The plus-end accumulation mechanism is understood only in *fungi,* mainly budding yeast[8, 21, 22, 23, 24, 25, 26, 27, 28] and, to a lower extend, fission yeast[29]. In budding yeast, dynein is targeted to the cortex through a threefold mechanism. Firstly, dynein is transported along astral microtubules pointing towards the bud by the kinesin kip2p and the microtubule associated protein (MAP) bik1p/CLIP170[24, 26, 27], whose closest homolog is CLIP-1 in *C. elegans*. Secondly, dynein accumulates at microtubule plus-ends both from transport along microtubules and directly from cytoplasm, in a bik1p/CLIP170 dependent fashion. Bik1p can either track directly microtubule plus-ends or use bim1p/EB, making this later dispensable[24, 28, 30]. Thirdly, dynein may also be targeted to the cortex without requiring microtubules and independently from Bik1p/CLIP170[23, 26, 27]. It is thought however that this third mechanism does not allow dynein to anchor to the cortex[8]. In contrast, in the two first mechanisms, once dynein reaches the bud, it is offloaded and anchored at the cortex by num1p, in a dynactin dependent manner[22]. However, in the second mechanism (direct accumulating to microtubule plus-ends), which is predominant[27], it is unclear whether dynein is transported (i.e. molecules moved towards the periphery) or simply gathered without displacing molecules. In contrast, in fission yeast, dynein diffuses along the microtubule lattice to reach the cortex[29]. Dynein accumulation at microtubule plus-ends, observed *in vivo* in HeLa cells[19] and mouse neuronal progenitor cells[31], is generally assumed to be caused by a mechanism related to the one shown in *fungi* although the details remains unclear.

During the asymmetric division of the *C. elegans* zygote, a limited number of active force generators[32, 33], whose engine is cortical dynein[34], pull on astral microtubules, causing forces that displace the spindle out-of-cell-center, in response to polarity cues[35]. This spindle posterior displacement together with elongation and anaphase spindle oscillations reveal the activity of the dynein at the cortex [32, 34, 36]. In this function, dynein belongs to the so-

called force generating complex, which also includes LIN-5/NuMA and GPR-1/2/LGN [37, 38]. This latter connects the complex to the cell membrane through Gα proteins[34] and could limit the number of active force generators[32, 33, 39, 40]. LIS-1 is eventually required also for all dynein functions[41]. In budding yeast, pac1p/LIS1 is required for targeting dynein[28], inhibiting it when it is not yet anchored[42]. This protein was also proposed to regulate dynein activity in other organisms[43]. Based on fine analysis of oscillations frequency, we previously hypothesized that cortical force generators pull for a very short time, 1s or less[44]. We could not distinguish in particular whether the unbalance of forces came from an asymmetry in the number of generators or in their dynamics.

Because dynein is essential to spindle positioning in higher eukaryotes, we asked by which mechanism it is targeted to the cortex and how this mechanism relates to the one shown in *fungi*. In particular, we wondered whether this mechanism is an auto-organization (passive) or an active transport (i.e. consuming energy like ATP). Here, we observed a fluorescently labeled DYCI-1, the sole homolog of IC, expressed under the endogenous promoter. We combined advanced image processing and fluorescence correlation spectroscopy (FCS) to analyze the dynamics of dynein *in vivo* during the first mitosis of *C. elegans* zygote. This approach enabled us to investigate dynamics in cytoplasm to address the cortex targeting mechanism but also dynamics at the cortex to decipher how the force asymmetry is encoded. We here sought to directly observe dynein dynamics at the cortex to support quantitative understanding of cell division mechanics.

Results

DYCI-1::mcherry is a *bona fide* reporter of dynein dynamics.

To investigate the *in vivo* dynamics of dynein targeting to the cortex and its residency there, we used a strain carrying a randomly integrated transgene coding for the mcherry fluorescently labeled dynein intermediate chain DYCI-1, expressed under its own promoter[45, 46]. This strain phenocopied N2 control strain. First, we wondered whether our construct was functional. Indeed, the transgene mostly rescued the null allele *dyci-1(tm4732)* (SI text §1.1.1-2). We concluded that despite an altered level of expression, DYCI-1::mcherry can perform native DYCI-1 functions.

We imaged this strain by spinning disk microscopy. We investigated dynamics both in a plane between the cover slip and the spindle, termed lower spindle plane (LSP) (Fig. 1D), and at the cortex. We revealed the motion of fluorescent spots by computing the standard deviation map (SDM, also called temporal variance image), which represents the intensity variation of each pixel over time[47] (SI methods). In the LSP, we observed both spindle and central spindle staining and spots moving radially towards the cortex during metaphase and anaphase (Fig. 1AB and S2AC, Movie S1 and S2). This is consistent with spindle and dotty cytoplasm localization previously revealed by antibody staining against dynein heavy chain DHC-1[34, 48] or CRISPR/Cas9-assisted labeling of the same subunit[49]. At the cell cortex, we observed transient spots (Fig. 1C, S2EG, Movie S3). Spots visible in LSP and at the cortex are not caused by over-expression: they were seen when only two copies of the transgene

were integrated by MosSCI[50, 51] even when endogenous *dyci-1* was suppressed through homozygous null allele *tm4732* (SI Text §1.1.3, Fig. S2BD, FH, Movies S4-5). We concluded that these spots are physiological. Their motion suggests that dynein is recruited at the microtubules lattice or at their plus-ends, like in yeast[27]. However, before investigating such an aspect, we validated our strain and developed the biophysics approach to go beyond the localization and address the mechanism, in particular whether it transport dynein and how it contributes to cortical force generation.

We next tested whether these spots could be stable aggregates. At the cortex, we analyzed their dynamics and observed a rapid turnover, in the order of the second, indicating that spots are dynamically forming and disappearing. In the LSP, since dynein may accumulate at microtubules as hypothesized from studies in budding yeast, spots lifetime may relate to the time during which a microtubule plus-end crosses the focal plane. Thus, we compared the spots assembly kinetics with the one of EB proteins at microtubule plus-ends[52]. We used a doubly labeled strain DYCI-1::mcherry EBP-2::GFP and measured spots intensity by FCS (Fluorescence Correlation Spectroscopy) in each channel (Fig. 3C). FCS enables to monitor diffusion in and out of a small volume. While both proteins are not associated in the cytoplasm as shown by FCCS (Fluorescence Cross Correlation Spectroscopy, monitoring co-diffusion of 2 labeled molecules in and out of the focal volume) (Fig. S1B), they shared a similar spot attachment kinetics (Fig S1C, SI text §1.1.5). We concluded that the DYCI-1::mcherry spots were dynamic both in LSP and at the cortex, which supports their biological relevance.

To prove that labeled dynein is involved in cortical pulling force generation, we used our previously published tube assay[33]: dyneins engaged in cortical pulling can create cytoplasmic membrane invaginations, especially upon depleting actin myosin cortex. Invaginations reveal the localization of pulling force generators, thus dynein. RNAi of force generators complex or related proteins significantly decrease the number of invaginations[33]. We crossed DYCI-1::mcherry and PH::GFP labeling strains (Fig. S3A), tracked DYCI-1::mcherry spots and observed that half of the invaginations colocalized with the resulting tracks (Movie S6, SI text §1.1.6) upon partial *nmy-2(RNAi),* to preserve polarity[33]. To test whether the invaginations abundance may cause artefactual colocalization, we compared with the colocalization of invaginations *versus* a distribution of the same number of simulated randomly localized spots (Fig. S3F) and found a very significant difference[53]. We concluded that colocalization was not artefactual. We performed similar controls in all further colocalizations. We attributed the lack of detection in half of the cases to the detection limit due to high DYCI-1::mcherry cytoplasmic fluorescence background. Indeed, we could estimate to 26 ± 4 dyneins per spot the threshold number to detect a spot above background (SI text §1.1.7). Dynein spots appeared typically 0.4 s earlier than the invagination (Fig. S3C-E, Movie S11), suggesting that dynein related pulling forces created the invagination. We concluded that DYCI-1::mcherry is part of dyneins involved in force generation.

DYCI-1 is the sole dynein intermediate chain in *C. elegans* and is already known to associate with two dynein complex subunits, DLC-1 and DYRB-1[54]. We wondered whether it remained associated with dynein all the time, and in particular in cytoplasm. We measured by fluorescence correlation spectroscopy (FCS) the diffusion coefficient of DYCI-1::mcherry and we obtained $D=2.6 \pm 0.7\ \mu m^2/s$ (N=9 embryos, 38 spots). It corresponds to the expected value for the whole dynein dimer, based on *in vitro* experiment[55] (SI Text §1.1.8). To gain further confidence, we partially depleted the light intermediate chain DLI-

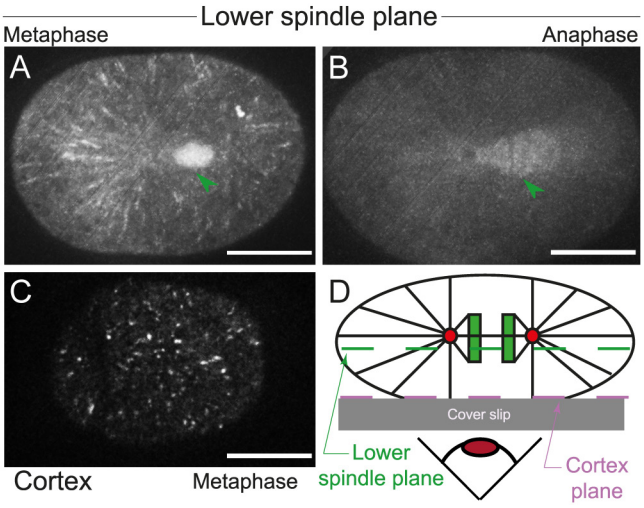

Figure 1: DYCI-1::mcherry in the cytoplasm, on the mitotic spindle and at the cell cortex.
Standard deviation map (SDM) computed over 30 frames from a 5 frames/s DYCI-1::mcherry movie taken (A) and (B) in lower spindle plane (LSP) during (**A**) metaphase, and (**B**) anaphase. (**C**) At the cell cortex during metaphase, DYCI-1::mcherry localized in a punctate manner. Green arrowheads indicate the mitotic spindle in LSP. Scale bars are 10 μm. (**D**) Schematic representation of the imaging setup.

1, essential to dynein function in the zygote[56] and observed no pronuclei meeting in 10/12 embryos. Furthermore, we fully lost the DYCI-1::mcherry spots present in non treated embryos at the same stage, which supports that DYCI-1::mcherry spots reveal dynein complexes. We concluded that detected DYCI-1::mcherry unravels dynein localization during the one cell embryo division, in particular cortical forces generation.

In the perspective of deciphering the mechanism of dynein targeting and its contribution to the pool of cortical pulling dyneins, we next wondered how many dyneins molecules are present in a single spot. We estimated the averaged number of dyneins using spot association kinetics equation fed with cytoplasmic concentrations (SI text §1.1.4) to cope with weak spots intensity precluding a direct measurement. We found 66 ± 5 dyneins per spot compared to 185 ± 85 EBP-2 per spot, in a strain carrying the randomly integrated DYCI-1::mcherry and EBP-2::GFP constructs (N=8 embryos, 38 spots). In the strain carrying two DYCI-1::mcherry copies on top of endogenous DYCI-1, we measured 29 ± 6 (N=5 embryos, 66 spots) dyneins per spot. Because this estimate is indirect, we sought a secondary and independent approach. We measured the intensity of dynein spots, background subtracted, and used par-6::mcherry strain background fraction to calibrate the intensity versus the number of particles by FCS (SI text §1.2.1, Fig. S10)[57]. We obtained 50 ± 13 particles per spot (N=6 embryos, 20 spots). This value is consistent with the previous estimate. Overall, our data show that randomly integrated DYCI-1::mcherry transgene, later referred simply as DYCI-1::mcherry, is a *bona fide* reporter of dynein, instrumental to report dynein dynamics both in cytoplasm and at the cortex.

Dynein spots displayed a directed (flow-like) motion towards periphery in the cytoplasm.

We observed spots of dynein moving towards cell periphery. We wondered what kind of mechanism was behind this and what would be its contribution to the regulation of cortical pulling forces. Various molecular mechanisms could be at work along or at the plus-end of microtubules, some being active transport (ATP dependent or more broadly consuming energy) and others relying on auto-organization using for example diffusion. we thus designed a pipeline to analyze the motion of DYCI-1::mcherry spots in LSP: (a) we denoised the image by using the CANDLE algorithm[58] (Fig. S4AB) and enhanced the spots

using the Laplacian of a Gaussian (LoG) (spot-enhancer)[59] (Fig. S4C); (b) we then tracked the image with u-track[60]; (c) we classified the tracks according to their motion, either anisotropic (termed "directed" for the sake of clarity and corresponding to transport or 1D diffusion) or isotropic (termed "diffusive-like", disregarding whether it is normal or anomalous)[61]; (d) we split directed tracks between those moving towards the cortex, and those moving towards the centrosome; (e) to foster a mechanistic approach, we applied a model based classification to directed tracks moving towards the cortex. We distinguished between diffusive motion (i.e. normal diffusion with linear relationship to time, even one-dimensional), "flow" (*sic*, transport like mechanism, excluding 1D diffusion) or a mixture of both. To do so, we used a Bayesian classification approach (BCA, SI text §1.3)[62]. To challenge this analysis pipeline, we used fabricated microscopy images at signal to noise ratios (SNR) similar to the experimentally observed ones (Fig. S5A-E, SI text §1.3.4) and successfully recovered the localization of the particles (Fig. S5H), speed and duration of trajectories (Fig. S5FG) and the classification between directed and diffusive-like trajectories (Fig. S5I). We analyzed dynein movies acquired in the LSP and found mostly directed tracks (Fig. 2AE, Fig. S8). Because tracks with diffusive-like motion last for shorter durations, we reasoned that they might be misclassified as diffusive-like disregarding their real motion. Supporting this possibility, the analysis of simulated data revealed that short tracks tended to be classified as diffusive-like disregarding their real motion (Fig. S5G). We also not further considered the rare tracks moving from the cortex to the centrosome in a directed motion. BCA on tracks directed towards the periphery revealed that the motion was likely a flow (Fig. 2F). Such a model is compatible with either an active transport of dynein along the microtubule lattice or an accumulation of dynein at microtubule plus-ends, for instance hitchhiking onto an EB homolog.

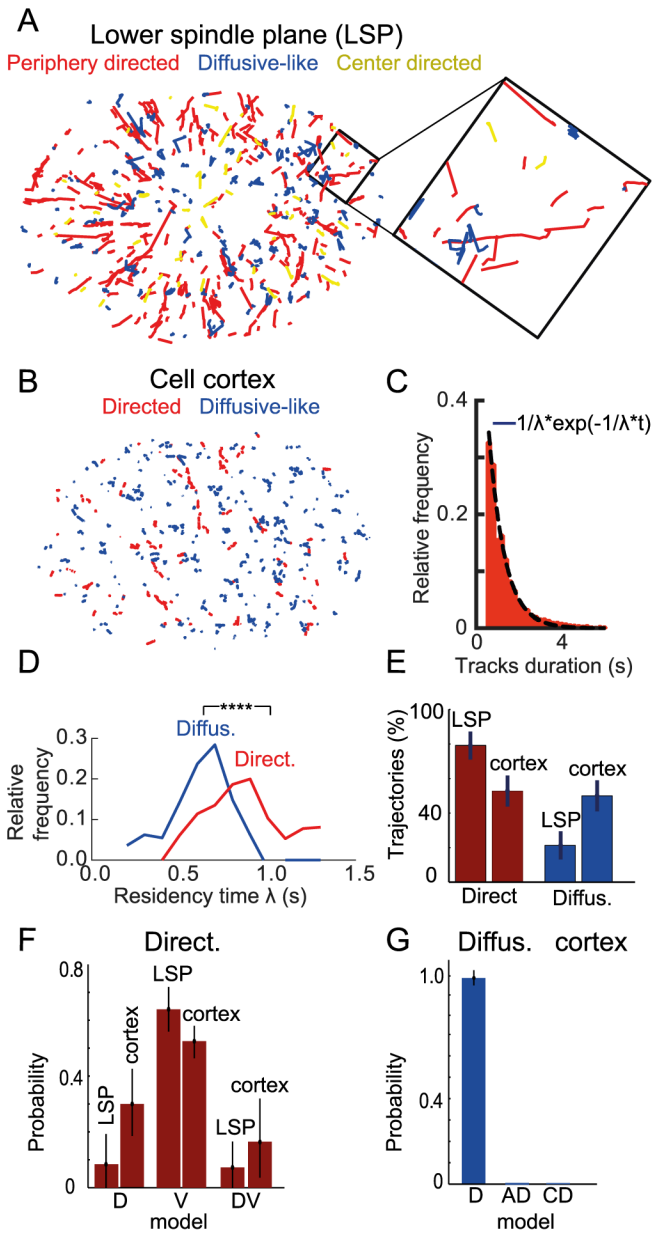

Figure 2: DYCI-1::mcherry exhibits different types of motion

(**A**) Tracks detected in LSP classified between directed towards the cell periphery (red), towards the center (orange) and diffusive-like (blue). Inset: zoom into a region highlighting the radial alignment of the directed tracks. (**B**) Tracks detected in a movie acquired at the cell cortex with similar color-coding. (**C**) Histogram of the tracks durations at the cell cortex for diffusive-like tracks of a typical embryo, fitted to an exponential with a residency time λ=0.7 s. (**D**) Distributions of the residency times λ for directed (red) and diffusive-like (blue) tracks at the cell cortex (N=26 embryos, 9595 tracks), displaying significantly different means. (**E**) Proportion of directed tracks moving towards the cortex (red) and diffusive-like (blue) tracks, in the LSP (left) and at the cortex (right), averaged over N=31 embryos (8060 tracks, LSP) and N=33 embryos (9921 tracks, cortex), respectively. (**F**) Probability of diffusive (D), flow (V) and mixture of both (DV) models computed on the directed towards the cortex (LSP, left) and directed (cortex, right) tracks using BCA (SI text §1.3.3) and averaged over N=31 embryos (5756 tracks, LSP) and N=33 embryos (4751 tracks, cortex). (**G**) Probability of diffusive (D), anomalous super-diffusion (AD) and confined diffusion (CD) models computed on the diffusive-like tracks at the cortex using BCA (N=33 embryos, 4874 tracks). 296 tracks at the cortex were too short to be classified (see suppl. Text). Error bars are s.e.m.

Dynein is accumulated at microtubule plus-ends, displaying dynamics similar to EBP-2/EB.

Directed motion of dynein spots towards the periphery could be active transport or passive microtubule plus-ends accumulation. We set to address this question by delineating the molecular players involved. It is likely that dynein localizes at the plus-ends based on studies in other organisms. The most studied plus-end–tracking proteins are EBs[63], whose homologs in nematode are is EBP-1/2/3, EBP-2 being the only one demonstrated to track plus-ends. We thus investigated dynein spots in comparison to it. We found that most of DYCI-1::mcherry spots colocalized with EBP-2::GFP in doubly labeled strain (Fig. 3AB and Movie S10). To gain further insight, we analyzed microtubules plus-ends crossing the FCS focal volume and detected coincident peaks for EBP-2::GFP and DYCI-1::mcherry (N= 8 embryos, 43 spots) (Fig. 3C)[52]. We wondered whether the spots not colocalized with

EBP-2::GFP could be along the microtubules lattice. We crossed strains carrying the DYCI-1::mcherry and α-tubulin::YFP transgenes and observed that DYCI-1 spots strongly colocalized with astral microtubules (Movie S9, Fig. S6B, SI text §1.2.2). The colocalized fraction was almost equal to the one of directed tracks towards the cell periphery and of colocalization with microtubule plus-ends. It suggests that the vast majority of DYCI-1::mcherry detectable spots colocalizes with EBP-2::GFP. We concluded that dynein and EB homolog EBP-2 share a common room at the microtubules growing plus-ends.

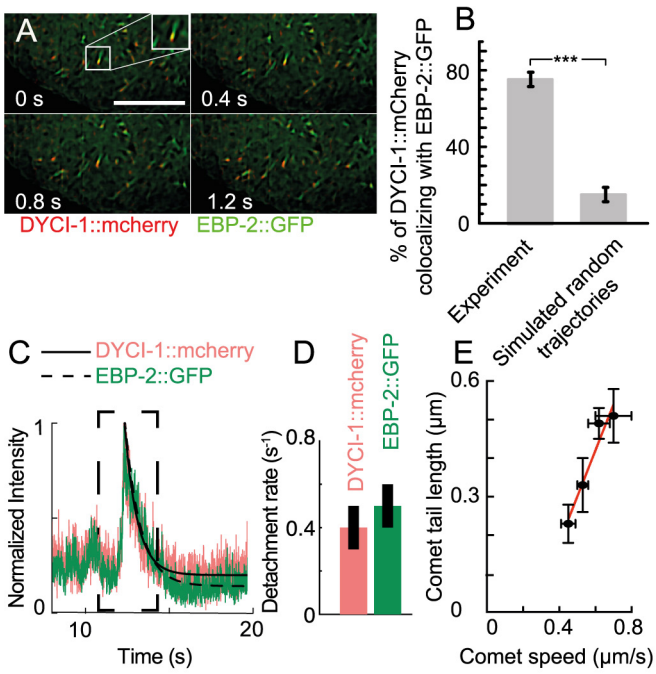

Figure 3: DYCI-1::mcherry colocalizes with EBP-2::GFP at the microtubule plus-ends.

(**A**) Sequence of micrographs of the metaphase of a *C. elegans* zygote, with DYCI-1::mcherry in red and EBP-2::GFP in green. Scale bar is 10 *µ*m. (**B**) Fraction in percent of DYCI-1::mcherry spots colocalizing with EBP-2::GFP (left, N=9 embryos, 1880 tracks) compared to colocalizing with simulated random trajectories (right, SI text § 1.2.2). Statistical significance was indicated by stars using Mann-Whitney/Wilcoxon test. (**C**) FCS of the intensity of DYCI-1::mcherry (red) and EBP-2::GFP (green), normalized by maximum, showing a spot crossing the focal volume. Black thin lines: exponential fits for DYCI-1::mcherry (plain line) and EBP-2::GFP (dashed line). The dashed rectangle indicates the coincident peaks. (**D**) Detachment rates for N=8 DYCI-1::mcherry ; EBP-2::GFP doubly labeled embryos, obtained by fitting 43 individual FCS traces as illustrated in (C). (**E**) Linear fit of DYCI-1::mcherry comet tail length (30-50 profiles per condition) versus comet speed (typically 7 embryos and 1500 trajectories per condition) for various microtubule growth rates (Fig. S6D) with slope=1.2 ± 0.2 s, significantly different from zero (p = 0.03) (SI text §1.2.3). Error bars are s.e.m.

We set to investigate the details of dynein accumulation at microtubule plus-end. Firstly, we wondered how dynein reaches the microtubule plus-ends. While validating the transgenic line, we found that microtubule plus-end binding kinetics of EBP-2::GFP and DYCI-1::mcherry were similar, depending exponentially upon the neighboring concentration (Fig. S1C)[52], while both proteins were dissociated in the cytoplasm (Fig. S1B). This suggests that dynein is recruited mostly from the cytoplasm. We next asked whether dynein was transported by the plus-end towards the cortex or just transiently associated to a tubulin dimer at the plus-end as EB proteins[64]. In the latter case, we expected the dynein spots to display a comet tail behavior reminiscent of the one observed for EB proteins[64]. Using FCS we measured an exponential decay of dynein intensity along the microtubule lattice from the plus-end (termed comet-tail, Fig. 3C). We repeated the experiment over several embryos and obtained similar detachment dynamic for DYCI-1::mcherry and EBP-2::GFP (Fig. 3D). It suggests a dynein dynamics at plus-end similar to EB one. To gain further insight, we noticed that a landmark of EB dynamics at microtubule plus-ends is the linear dependence of the physical extends of this comet-tail upon the growth rate of microtubules, which proves that EB is not actively transported but only bound to a tubulin dimer. We set to perform such an experiment on DYCI-1::mcherry by modulating

microtubule dynamics through hypomorphic *klp-7(RNAi)* or *clip-1(RNAi)* (typically N=7 embryos, 1500 tracks per condition) (SI text §1.2.3 and Fig. S1A). Penetrant depletion of these genes did not preclude dynein recruitment at plus-ends (Fig. 5AB). We found in DYCI-1::mcherry strain a linear relation between comet-tail and growth rate, with a slope 1.2 ± 0.2 s, significantly different from zero (p=0.03) (Fig. 3E). Because dynein shows similar binding and unbinding dynamics at microtubule plus-ends as EB proteins, we concluded that dynein is not actively transported by microtubule plus-ends but only accumulated there, as is EBP-2/EB[64], putatively hitchhiking on this latter protein.

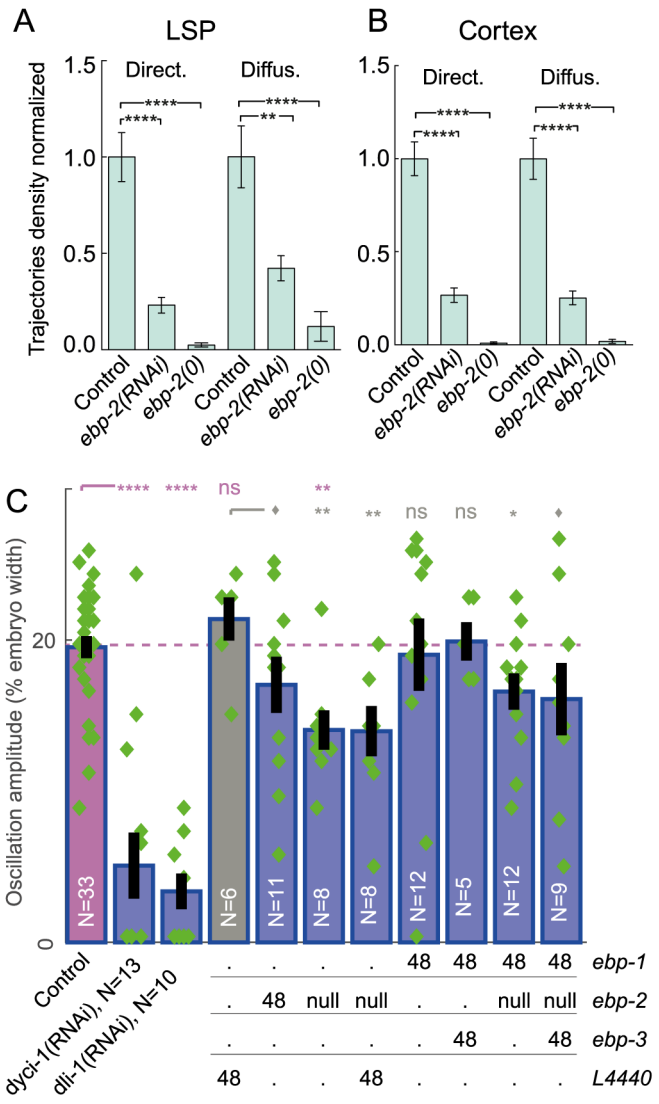

Figure 4: EBP-2 contributes to accumulating DYCI-1::mcherry to the microtubule +TIPs.

(**A** and **B**) Trajectories density normalized by the median in corresponding control for DYCI-1::mcherry (A) in the LSP and (B) at cell cortex, in control, upon partial *ebp-2(RNAi)* and crossing with null mutation *ebp-2(gk756)*. Error bars are s.e.m. Data in LSP from N=8 control, 11 *ebp-2(RNAi)*, 5 *ebp-2(gk756)* embryos, and at the cortex from N=6, 9 and 3 embryos, respectively. (**C**) Anaphase posterior centrosome oscillations maximum amplitude in % of embryo width upon various depletions of EB homologs EBP-1/2/3 and DYCI-1 or DLI-1 partial depletions for reference. Table below the plot indicates conditions: *null* for null mutant *ebp-2(gk756)*, numbers of hours of feeding in RNAi experiments. Green diamonds correspond to raw data and black error bars to s.e.m. Horizontal dashed line indicates the amplitude for non-treated embryos. Pink stars indicate significance with respect to non-treated embryos and grey ones with respect to control RNAi with L4440 vector.

Dynein accumulates at microtubule plus-ends in an EBP-2, Dynactin and LIS-1 dependent fashion but independently from EBP-1/-3, CLIP-1/CLIP170 and likely kinesins.

In budding yeast, dynein is recruited at microtubule plus-ends in a pac1p/LIS-1 and bik1p/CLIP-1 dependent manner[8, 9, 23, 24, 25, 26, 27, 28, 30]. In higher eukaryotes, dynactin has

been proposed to take part in the hierarchical interaction at plus-ends connecting dynein and EB, based on *in vitro* experiments using purified human proteins[65]. To test whether such plus-end accumulation mechanism exists in the nematode, we depleted EBP-2 by RNAi and observed in the LSP a severe decrease of the density of dynein directed (and diffusive) tracks (Fig. 4A, Fig. S7A) while no alteration was observed for the diffusion coefficient of dyneins in the cytoplasm (Fig. S7B). We confirmed this result by crossing the DYCI-1::mcherry strain with a strain carrying the null mutation *ebp-2(gk756)*: we obtained a viable strain displaying no dynein spot in the cytoplasm (Fig. 4A). From direct observation of the images, we cannot exclude that some faint spots are still present at the cortex ; their detection would require more permissive processing pipeline parameters that would be prone to artifacts. Similarly, we observed a strong reduction of the density of directed tracks in the LSP upon depletion of dynactin by *dnc-1(RNAi)*, homolog of p150glued, and *lis-1(RNAi)* (Fig. 5A, Fig. S7C-E). Indeed, depletion of any of them results in a strong phenotype, reminiscent of dynein depletion[41, 66]. Surprisingly, *clip-1(RNAi)* resulted in no significant alteration of dynein tracks density (Fig. 5A). We confirmed this result by crossing the DYCI-1::mcherry strain with a strain carrying the null mutation *clip-1(gk470)*: tracks density was not decreased (Fig. 5A). Since dynein is needed to generate forces that position the spindle, reflected by anaphase oscillations[3, 44, 48], a defect in dynein targeting to the cell cortex is expected to strongly reduce these oscillations, similarly to *gpr-1/2(RNAi)* or *dli-1(RNAi)*[44]. We crossed a centrosomes labeled γTUB::GFP carrying strain with *clip-1(gk470)* and measured no significant reduction of anaphase oscillations amplitude (Fig. S9B). We concluded that the mechanism targeting dynein to microtubule plus-ends shows similarities with the mammalian one involving EB, Dynactin and LIS1 homologs. However, it seemed not to involve CLIP-1/CLIP170.

EBP-2 contributes to accumulating dynein at microtubule plus-ends but surprisingly *epb-2(RNAi)* was reported as having no early embryonic phenotype[17, 67]. We tracked the γTUB::GFP labeled posterior centrosome and analyzed its oscillations upon *ebp-2(RNAi)* or in null mutant *ebp-2(gk756)*. Oscillations were reduced but not abolished (Fig. 4C). Because *C. elegans* has three homologs of EB proteins, all with no early embryonic phenotype[17, 67], we tested a putative redundancy. We treated null mutants *ebp-2(gk756)* with *ebp-1(RNAi)* or *ebp-1/-3(RNAi)* using a single transcript, but found no further reduction of the oscillation amplitude (Fig. 4C). Consistently, it has been suggested that dynein is still localized at the microtubules plus-ends in absence of EBP-1/3[49]. We concluded that EBP-2, but not EBP-1 or EBP-3, is likely involved in targeting dynein to the cortex by contributing to the accumulation of dynein at the astral microtubules plus-ends. Furthermore, because some pulling force persisted in absence of EBP-2, we suggest that a partially redundant mechanism is likely to exist.

The EBP-2 dependent mechanism accumulating dynein at microtubule plus-ends does not account fully for dynein targeting to the cell cortex. In budding yeast, kinesin kip2p (no known homolog in *C. elegans*) is involved in a mechanism transporting dynein along microtubules[8, 26, 27]. Phenotypic screens performed in nematode suggest however that no kinesin RNAi cancels out anaphase oscillations[17, 67]. Our experiments suggest that only klp-13, -18, -19, -20 mildly and non-significantly decrease oscillations amplitude upon depletion (Fig. S9A, SI text §1.2.4). Klp-18 was previously reported as playing no role in mitosis[68]. Depletion of the 3 other kinesins, which resulted in a mild oscillations amplitude decrease, did not reduce dynein accumulation at microtubule plus-end (Fig. 5B). In conclusion, it is likely that kinesins do not contribute to transporting dynein to the cortex during one-cell embryo division.

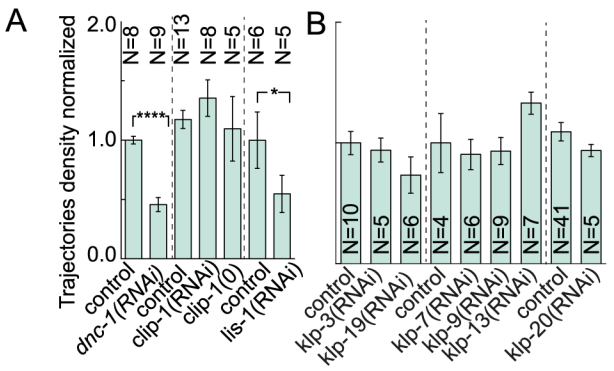

Figure 5: DYCI-1::mcherry dynamics depends on dynactin, LIS-1 but not CLIP-1 nor kinseins
Normalized trajectories density of DYCI-1::mcherry in the LSP in control and upon partial RNAi of (**A**) *dnc-1, clip-1, lis-1* and crossing with null mutant *clip-1(gk470)* as well as (**B**) selected kinesins. No significant difference was found for the kinesins and CLIP-1. Error bars are s.e.m.

Dynamics of DYCI-1::mCherry at the cell cortex: dynein–microtubule on-rate antero-posterior asymmetry likely account for cortical pulling forces imbalance.

When dynein reaches the cell cortex, it is offloaded to take part in force generation. We imaged and tracked DYCI-1::mcherry labeled dynein at the cortex (SI text §1.2.5) and found, in contrast with the results in the LSP, equal proportions of directed and diffusive-like tracks, both residing less than 1 second (Fig. 2BD). Consistently, we found that diffusive-like (anisotropic) tracks displayed a diffusive motion in BCA model classification (Fig. 2G). We wondered whether cortical dynein spots are related to the ones in the cytoplasm. We analyzed cortical spot upon *ebp-2(RNAi)* or crossing to null *ebp-2* mutant: we found a drastic reduction of the track density as observed in the LSP (Fig. 4B, S7F-I). It suggests that dynein accumulated at microtubule plus-ends was offloaded to the cortex as in budding yeast[8, 22]. However, we did not focus on the molecular details of offloading but rather on the dynamics of dynein at the cortex in relation with asymmetric forces generation that we have previously modeled[44].

An asymmetric distribution of active force generators pulling on astral microtubules posteriorly displaces the spindle during anaphase in the *C. elegans* zygote[32, 44]. It is very likely that the force generators are cytoplasmic dyneins[34, 44]. Their asymmetric activity could arise from 3 mechanisms: (1) a posterior enrichment (number asymmetry) either due to a larger total number of dyneins (active and inactive) or due to an increased on-rate, i.e. a higher rate of capture of an astral microtubule by a dynein at the cortex to pull on it ; (2) an asymmetry in time spent pulling on microtubule (processivity) before leaving the cortex, related to the residency time at the cortex; or (3) a differential regulation of dynein force generation through accessory proteins. We analyzed dynein tracks within 4 regions of equal extend along the antero-posterior axis (Fig. 6E) and observed a higher density on posterior tip compared to anterior one (Fig. 6CD, green lines) both for directed and diffusive-like tracks. To test whether more dynein (active and inactive) could arrive and then be present at the posterior cortex, we computed the posterior to anterior ratio of tracks in the LSP and obtained 0.95 ± 0.09 for directed tracks and 1.0 ± 0.1 for diffusive like (N=7 embryos, 1341 tracks). This suggests that an equal flux of dynein is likely to reach both cortex halves, suggesting that force imbalance is more likely due to an asymmetry of dynein–microtubule on-rate. It was however somewhat surprising that the two middle regions have the highest densities of microtubules. We attributed this result to the reduced number of (long) microtubule reaching the tips of the embryo[40, 69] as we imaged during metaphase and the spindle was only slightly displaced towards the posterior. We next wondered whether these asymmetric density of dynein depends on GPR-1/2, subunits of the cortical force generating complex and known to have an asymmetric distribution[39, 40]. We depleted this

protein by RNAi and observed a proportional decrease of the densities in each region for diffusive tracks. The effect was much less pronounced on directed tracks and restricted to the posterior region (Fig. 6CD, purple lines). In both cases, it will decrease the asymmetry. We concluded that GPR-1/2 is likely to contribute to cortical pulling force imbalance through enhancing dynein–microtubule on-rate.

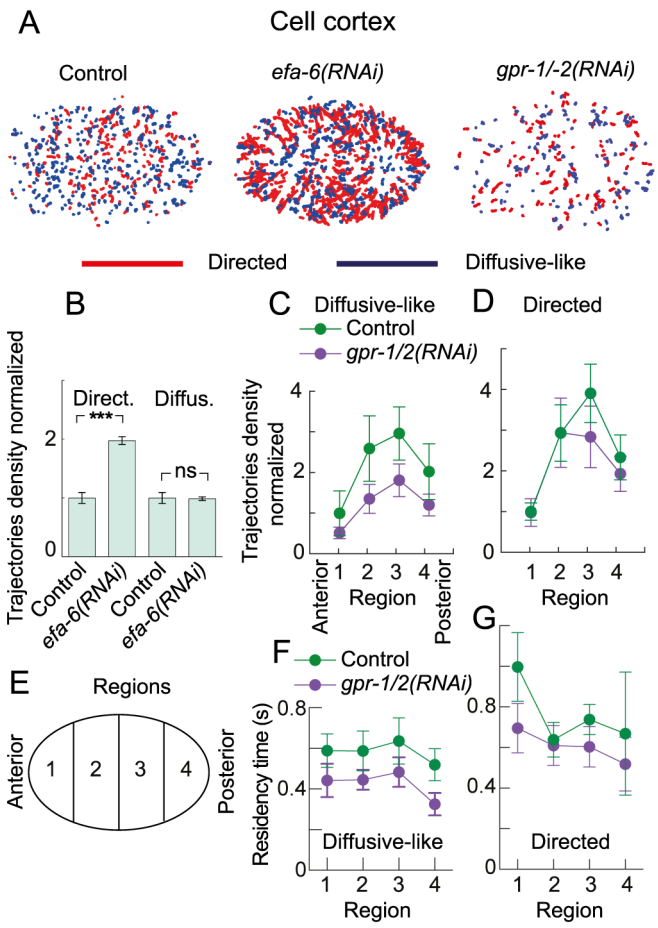

Figure 6: EFA-6 and GPR-1/-2 regulate DYCI-1::mcherry dynamics at the cell cortex.

(**A**) Tracks detected at the cell cortex in (left) control, (middle) *efa-6(RNAi)* and (right) *gpr-1/-2(RNAi)* treated embryos. Tracks were classified between (red) directed and (blue) diffusive-like. (**B**) Normalized tracks densities at the cell cortex in N=7 control (3000 tracks) and N=9 *efa-6(RNAi)* treated (1400 tracks) embryos. **(CD)** Diffusive-like and directed track densities at the cell cortex, analyzed within four regions of equal length along AP axis (see E) in control and *gpr-1/2(RNAi)* treated DYCI-1::mcherry embryos. (**E**) Schematics of the 4 regions. **(FG)** Residency times corresponding to (CD). We analyzed N=7 control (1740 tracks) and N=11 *gpr-1/-2(RNAi)* treated (2120 tracks) embryos. Error bars are s.e.m.

Force generators processivity (inverse of the off-rate) was proposed to regulate the cortical pulling forces during anaphase[44]. We thus set to measure residency times of dynein in the same setup (Fig. 6FG) through fitting the histogram of dynein tracks duration (Fig. 2CD). We noticed no asymmetry in control embryos and *gpr-1/2(RNAi)* resulted into an overall reduction. We concluded that GPR-1/2 enhanced force generators processivity[32, 44], although there is no asymmetry in force generator processivity in contrast with dynein density.

It is interesting to notice that the reduction of force generation through *gpr-1/2(RNAi)* mostly affected the diffusive population, suggesting a link between this one and force generating events. Because dynein spots displayed mostly a directed motion in the cytoplasm, we reasoned that directed tracks might correspond to dynein spots finishing to arrive at the cortex on a microtubule plus-end and not to dynein residing there. Indeed, the thickness of the imaged volume could include the sub-cortical region where the microtubule can grow despite the optical sectioning of the spinning disk microscope. Consistently, BCA analysis applied to directed tracks provided motion probabilities similar to the ones obtained in the LSP (Fig. 2F). To test whether directed tracks relate to

microtubule growing to the cortex, we depleted EFA-6, a putative microtubule regulator limiting their growth, using RNAi. We observed that directed tracks were longer along the cortex, as expected (Fig. 6A, middle)[70]. Directed tracks were also more numerous than in control, while the diffusive-like population was not significantly affected (Fig. 6AB). We concluded that directed tracks are likely to correspond mainly to dynein at plus-ends for microtubules arriving at the cortex.

Discussion

Using the fluorescently labeled dynein subunit DYCI-1 as a *bona fide* reporter of dynein, we developed a method enabling to analyze the dynamics of dynein. We applied it both in the cytoplasm and at the cell cortex: in the former (LSP), we found that dynein was accumulated at the microtubule plus-ends in an EBP-2/EB, dynactin and LIS-1 dependent fashion but independently of CLIP-1/CLIP170 and kinesins. Supports were fourfold: firstly, dynein spots colocalized with EBP-2 at microtubule plus-end; secondly, their dynamics followed the one of microtubules; thirdly, they displayed an attachment/detachment dynamics similar to EBP-2; and fourthly, depletion of the above proteins reduced or suppressed the dynein plus-end accumulation. However, dynein was not actively transported towards the cell periphery (discussed below). At the cortex, we found two populations of dynein: one with a directed motion, residing longer at the cortex and attributed to microtubule plus-ends finishing their approach to the cortex; one shorter-residing and displaying a diffusive-like motion, which may correspond to pulling force generating events, i.e. the dyneins contributing to cortical pulling observed right at the time of force generation.

The set of involved proteins in dynein plus-end accumulation is not fully consistent with hierarchical interactions based on *in vitro* minimal system using human proteins[65]. Indeed, CLIP-1/CLIP170 plays no role in the nematode and some cortical pulling forces remain upon suppression of EBP-2/EB. In budding yeast, bim1p/EB is also dispensable but in contrast to the nematode, plus-end accumulations are preserved when bim1p is suppressed, relying on bik1p/CLIP170 ability to track plus-end. Bik1p/CLIP170 is not dispensable in budding yeast[24, 28, 30] while CLIP-1/CLIP170 suppression did not reduce plus-end accumulation or cortical forces in nematode. Indeed, the weak homology between CLIP-1 and mammalian CLIP170 could be explicative[71]: it has recently been proposed to rather be a tubulin folding cofactor B[72]. In conclusion, dynein tracking of microtubule plus-ends in nematode appeared related but not similar to previously studied organisms.

Why were cortical forces partially preserved upon EBP-2/EB suppression despite plus-ends accumulation disappearance? We hypothesized that this apparent contradiction between localization and functional results was due to a secondary mechanism, partially redundant, targeting dynein to the cortex. We found no indication that kinesins may be involved. On top of the functional approach, it is noteworthy that a kinesin contributing to targeting dynein to the microtubule plus-ends would have produced different attachment kinetics from the one we observed and that mimicked EBP-2/EB: it would have followed the antenna model in which microtubule collects protein that can then diffuse in 1D to the plus-end[73, 74]. Excluding a contribution of CLIP-1 (redundant mechanism for plus-end

accumulation), kinesins (transport along microtubule) and microtubule lattice diffusion, we considered dynein diffusion in 3D as a putative secondary mechanism. Indeed, by FCS, we measured a high cytoplasmic concentration, 177 ± 60 nM (i.e. 32 ± 11 molecules in FCS focal volume of 0.3 fl, N=8 embryos, 38 spots, SI text §1.1.4). We can estimate that this could account for a rate of about 30 dynein molecules per second reaching a half cortex (SI text §1.2.6)[75]. We cannot decide which proportion of these is active. However and although the value is bit small, it is consistent with 10 to 100 active force generators per half cortex[32] staying about 0.5 s. In conclusion, 3D diffusion is the most plausible secondary mechanism. Interestingly, NuMA homolog LIN-5, part of the cortical force generating complex, was proposed to recruit dynein at the cortex independently of astral microtubules[49].

The asymmetric positioning of the spindle during the division of the *C. elegans* zygote relies on an imbalance of cortical forces, stronger on posterior[32, 44]. This is mediated by proteins GPR-1/2, possibly through their concentration at the posterior tip of the cortex[39, 40]. We suggest here that GPR-1/2 asymmetric localization causes asymmetric densities of dynein spots. Because no posterior/anterior asymmetry was observed in the cytoplasm, we suggest that the same number of dyneins is arriving at the cortex on both side and that their total number at the cortex is the same. The asymmetric density arises from different binding rate to the other parts of the force generating complex and/or microtubule, i.e. an asymmetry in engaging in cortical pulling.

Dynein turnover at the cortex is extremely fast with a residency time below 1s, which offers adaptive localizing in response to spindle internal and dynamic polarity cues[40, 76, 77]. This is also consistent with the short run-time, about 0.5 s, during which force generators (dyneins) are engaged in pulling on astral microtubule, after the modeling of anaphase centrosome oscillations[44]. Interestingly, GPR-1/2 also contributes to the increase of the processivity of the force generators, in a non polarized fashion, as revealed by dyneins residency time. Regulation of processivity is likely the mean by which the force increases along the course of mitosis[44]. We suspect this role of GPR-1/2 to be indirect, putatively because GPR-1/2 would be needed to regulate localization or activation of other member of force generation complex and by this way regulating processivity

We measured at the cortex two populations of dyneins dynamically distinct. We propose that the diffusive-like population participates in force generating events. First, the observed residency time is consistent with the short residency times measured for microtubules[69] and with the estimated force generator run-time from modeling anaphase centrosomes oscillations[44]. Second, the count of spots is consistent with the expected number of active force generators[32, 33]. Indeed, we observed about 0.008 diffusive tracks per μm^2 of visible cortex area (instantaneous density) in the posterior half, meaning about 20 diffusive tracks in the posterior half cortex at any instant. This is consistent with the expected 10-100 forces generators per half cortex (Grill et al., 2003). Third, this population is altered upon targeting the force generating complex through *gpr-1/2(RNAi)*. It is unlikely that diffusive-like spots also include microtubule plus-ends diffusing at the cortex to "search" for a force generator anchorage[6] since the diffusive-like population is not dependent upon microtubule growing dynamics, as suggested by our *efa-6(RNAi)* experiment. In contrast, "searching" microtubules may belong to the directed population at the cortex and can account for its longer residency time. Alternatively, the longer residency times of directed tracks may also correspond to dynein spots that supplement a directed motion, finishing to

arrive to the cortex, with a diffusive motion during a shorter time (e.g. a brief force generating event).

In conclusion, dynein displays a high dynamics at the cell cortex requiring a highly efficient targeting mechanism. Diffusion in the cytoplasm is reinforced by the accumulation of dynein at the microtubule plus-ends, where it is hitchhiking on EBP-2 with the help of dynactin and LIS-1. However, as for cytoplasm diffusion, this mechanism is not actively transporting dynein but only concentrates it at microtubule plus-ends. Although not an active transport, this mechanism is useful: to generate pulling forces, a microtubule plus-end, a dynein-dynactin complex, GPR-1/2 and LIN-5 need to meet ; they have a one second-long delay to create the force generating complex. In this perspective, having gathered dynein and microtubule beforehand is of help and calls for further exploration of the offloading details in future studies. Alternatively, the growing plus-ends, through binding/unbinding dyneins, can bias the diffusion of these latter in the cytoplasm, favoring motions toward the cortex.

Acknowledgements

We thank Prof. Anthony A. Hyman and Dr Mihail Sarov for strains, in particular the kind gift of the randomly integrated DYCI-1::mcherry TH163, Dr J.W. Dennis for DE74 strain, Dr S. Redemann for preliminary data on this project, Drs N. Monnier and M. Bathes for support in applying Bayesian analysis, Dr G. Michaux for feeding clones library, B. Mercat and Drs A. Pacquelet, X. Pinson, H. Bouvrais, Y. Le Cunff, G. Michaux, R. Le Borgne, S. Huet for technical help, critical comments on the manuscript and discussions about the project. RRG and JP were supported by a CNRS ATIP starting grant and la ligue nationale contre le cancer. Some strains were provided by the CGC, which is funded by NIH Office of Research Infrastructure Programs (P40 OD010440; University of Minnesota, USA), the National Bio-resource Project (Tokyo University, Japan), and the *C. elegans* Gene Knockout Consortium. MosSci strain was made by the "Biology of *Caenorhabditis elegans*" facility UMS 3421, CNRS / UCBL (Lyon, France). Microscopy imaging was performed at the MRIC facility, UMS 3480 CNRS / US 18 INSERM / Univ. Rennes 1. FCS microscopy setup was funded by ARC grant # EML20110602452. Spinning disk was co-funded by CNRS, Rennes métropole and region Bretagne (grant AniDyn-MT).

Author contributions

RRG, LC and JP designed the research, analyzed the data and wrote the paper; RRG, LC, SP performed the research. JR and MT contributed new analytic tools.

References

1. Gonczy P, Pichler S, Kirkham M, Hyman AA. Cytoplasmic dynein is required for distinct aspects of MTOC positioning, including centrosome separation, in the one cell stage Caenorhabditis elegans embryo. *J Cell Biol* **147**, 135-150 (1999).

2. Dujardin DL, Vallee RB. Dynein at the cortex. *Current opinion in cell biology* **14**, 44-49 (2002).

3. Nguyen-Ngoc T, Afshar, K., and Gonczy, P. Coupling of cortical dynein and G alpha proteins mediates spindle positioning in Caenorhabditis elegans. Nat. Cell Biol. *9* **1294-1302**, (2007).

4. Karki S, Holzbaur EL. Cytoplasmic dynein and dynactin in cell division and intracellular transport. *Current opinion in cell biology* **11**, 45-53 (1999).

5. Kotak S, Gonczy P. Mechanisms of spindle positioning: cortical force generators in the limelight. *Current opinion in cell biology* **25**, 741-748 (2013).

6. Laan L*, et al.* Cortical dynein controls microtubule dynamics to generate pulling forces that position microtubule asters. *Cell* **148**, 502-514 (2012).

7. Carminati JL, Stearns T. Microtubules orient the mitotic spindle in yeast through dynein-dependent interactions with the cell cortex. *J Cell Biol* **138**, 629-641 (1997).

8. Markus SM, Lee WL. Regulated offloading of cytoplasmic dynein from microtubule plus ends to the cortex. *Dev Cell* **20**, 639-651 (2011).

9. Moore JK, Li J, Cooper JA. Dynactin function in mitotic spindle positioning. *Traffic* **9**, 510-527 (2008).

10. Shaw SL, Yeh E, Maddox P, Salmon ED, Bloom K. Astral microtubule dynamics in yeast: a microtubule-based searching mechanism for spindle orientation and nuclear migration into the bud. *J Cell Biol* **139**, 985-994 (1997).

11. Collins ES, Balchand SK, Faraci JL, Wadsworth P, Lee WL. Cell cycle-regulated cortical dynein/dynactin promotes symmetric cell division by differential pole motion in anaphase. *Mol Biol Cell* **23**, 3380-3390 (2012).

12. McNally FJ. Mechanisms of spindle positioning. *J Cell Biol* **200**, 131-140 (2013).

13. King SM. *Dyneins : structure, biology and disease*, 1st edn. Academic Press (2012).

14. Pfister KK, Lo KW-H. Cytoplasmic Dynein Function Defined by Subunit Composition. In: *Dyneins : structure, biology and disease* (ed^(eds King SM). 1st edn. Academic Press (2012).

15. Pfister KK*, et al.* Genetic analysis of the cytoplasmic dynein subunit families. *PLoS Genet* **2**, e1 (2006).

16. King SM. AAA domains and organization of the dynein motor unit. *J Cell Sci* **113 (Pt 14)**, 2521-2526 (2000).

17. Sonnichsen B*, et al.* Full-genome RNAi profiling of early embryogenesis in Caenorhabditis elegans. *Nature* **434**, 462-469 (2005).

18. Kamath RS, Ahringer J. Genome-wide RNAi screening in Caenorhabditis elegans. *Methods* **30**, 313-321 (2003).

19. Kobayashi T, Murayama T. Cell cycle-dependent microtubule-based dynamic transport of cytoplasmic dynein in mammalian cells. *PLoS ONE* **4**, e7827 (2009).

20. Splinter D*, et al.* BICD2, dynactin, and LIS1 cooperate in regulating dynein recruitment to cellular structures. *Mol Biol Cell* **23**, 4226-4241 (2012).

21. Moore JK, Stuchell-Brereton MD, Cooper JA. Function of dynein in budding yeast: mitotic spindle positioning in a polarized cell. *Cell Motil Cytoskeleton* **66**, 546-555 (2009).

22. Lee WL, Kaiser MA, Cooper JA. The offloading model for dynein function: differential function of motor subunits. *J Cell Biol* **168**, 201-207 (2005).

23. Sheeman B*, et al.* Determinants of S. cerevisiae dynein localization and activation: implications for the mechanism of spindle positioning. *Curr Biol* **13**, 364-372 (2003).

24. Carvalho P, Gupta ML, Jr., Hoyt MA, Pellman D. Cell cycle control of kinesin-mediated transport of Bik1 (CLIP-170) regulates microtubule stability and dynein activation. *Dev Cell* **6**, 815-829 (2004).

25. Lee WL, Oberle JR, Cooper JA. The role of the lissencephaly protein Pac1 during nuclear migration in budding yeast. *J Cell Biol* **160**, 355-364 (2003).

26. Roberts AJ, Goodman BS, Reck-Peterson SL. Reconstitution of dynein transport to the microtubule plus end by kinesin. *eLife* **3**, e02641 (2014).

27. Markus SM, Punch JJ, Lee WL. Motor- and tail-dependent targeting of dynein to microtubule plus ends and the cell cortex. *Curr Biol* **19**, 196-205 (2009).

28. Markus SM, Plevock KM, St Germain BJ, Punch JJ, Meaden CW, Lee WL. Quantitative analysis of Pac1/LIS1-mediated dynein targeting: Implications for regulation of dynein activity in budding yeast. *Cytoskeleton (Hoboken)* **68**, 157-174 (2011).

29. Ananthanarayanan V, Schattat M, Vogel SK, Krull A, Pavin N, Tolic-Norrelykke IM. Dynein motion switches from diffusive to directed upon cortical anchoring. *Cell* **153**, 1526-1536 (2013).

30. Caudron F, Andrieux A, Job D, Boscheron C. A new role for kinesin-directed transport of Bik1p (CLIP-170) in Saccharomyces cerevisiae. *J Cell Sci* **121**, 1506-1513 (2008).

31. Molina-Calavita M, Barnat M, Elias S, Aparicio E, Piel M, Humbert S. Mutant huntingtin affects cortical progenitor cell division and development of the mouse neocortex. *J Neurosci* **34**, 10034-10040 (2014).

32. Grill SW, Howard J, Schaffer E, Stelzer EH, Hyman AA. The distribution of active force generators controls mitotic spindle position. *Science* **301**, 518-521 (2003).

33. Redemann S*, et al.* Membrane invaginations reveal cortical sites that pull on mitotic spindles in one-cell C. elegans embryos. *PLoS One* **5**, e12301 (2010).

34. Nguyen-Ngoc T, Afshar K, Gonczy P. Coupling of cortical dynein and G alpha proteins mediates spindle positioning in Caenorhabditis elegans. *Nat Cell Biol* **9**, 1294-1302 (2007).

35. Colombo K, Grill SW, Kimple RJ, Willard FS, Siderovski DP, Gonczy P. Translation of polarity cues into asymmetric spindle positioning in Caenorhabditis elegans embryos. *Science* **300**, 1957-1961 (2003).

36. Rose L, Gonczy P. Polarity establishment, asymmetric division and segregation of fate determinants in early C. elegans embryos. *WormBook*, 1-43 (2014).

37. Srinivasan DG, Fisk RM, Xu H, van den Heuvel S. A complex of LIN-5 and GPR proteins regulates G protein signaling and spindle function in C elegans. *Genes Dev* **17**, 1225-1239 (2003).

38. Galli M*, et al.* aPKC phosphorylates NuMA-related LIN-5 to position the mitotic spindle during asymmetric division. *Nat Cell Biol* **13**, 1132-1138 (2011).

39. Park DH, Rose LS. Dynamic localization of LIN-5 and GPR-1/2 to cortical force generation domains during spindle positioning. *Dev Biol* **315**, 42-54 (2008).

40. Riche S, Zouak M, Argoul F, Arneodo A, Pecreaux J, Delattre M. Evolutionary comparisons reveal a positional switch for spindle pole oscillations in Caenorhabditis embryos. *J Cell Biol* **201**, 653-662 (2013).

41. Cockell MM, Baumer K, Gonczy P. lis-1 is required for dynein-dependent cell division processes in C. elegans embryos. *J Cell Sci* **117**, 4571-4582 (2004).

42. Lammers LG, Markus SM. The dynein cortical anchor Num1 activates dynein motility by relieving Pac1/LIS1-mediated inhibition. *J Cell Biol* **211**, 309-322 (2015).

43. Trokter M, Surrey T. LIS1 Clamps Dynein to the Microtubule. *Cell* **150**, 877-879 (2012).

44. Pecreaux J*, et al.* Spindle oscillations during asymmetric cell division require a threshold number of active cortical force generators. *Curr Biol* **16**, 2111-2122 (2006).

45. Sarov M*, et al.* A genome-scale resource for in vivo tag-based protein function exploration in C. elegans. *Cell* **150**, 855-866 (2012).

46. Sarov M*, et al.* A recombineering pipeline for functional genomics applied to Caenorhabditis elegans. *Nat Methods* **3**, 839-844 (2006).

47. Rostampour AR, Reeves AP, Mitchell OR. Use of temporal variance for moving object extraction. In: *Computers and Communications, 1988. Conference Proceedings., Seventh Annual International Phoenix Conference on* (ed^(eds) (1988).

48. Gonczy P, Pichler S, Kirkham M, Hyman AA. Cytoplasmic dynein is required for distinct aspects of MTOC positioning, including centrosome separation, in the one cell stage Caenorhabditis elegans embryo. *J Cell Biol* **147**, 135-150 (1999).

49. Schmidt R, A A, Heuvel Svd. Spindle positioning in the C. elegans zygote in the absence of EBPs and dynein plus-end tracking. *submitted*, (2016).

50. Boulin T, Bessereau JL. Mos1-mediated insertional mutagenesis in Caenorhabditis elegans. *Nat Protoc* **2**, 1276-1287 (2007).

51. Robert V, Bessereau JL. Targeted engineering of the Caenorhabditis elegans genome following Mos1-triggered chromosomal breaks. *Embo J* **26**, 170-183 (2007).

52. Dragestein KA*, et al.* Dynamic behavior of GFP-CLIP-170 reveals fast protein turnover on microtubule plus ends. *J Cell Biol* **180**, 729-737 (2008).

53. Jaqaman K*, et al.* Cytoskeletal control of CD36 diffusion promotes its receptor and signaling function. *Cell* **146**, 593-606 (2011).

54. Boxem M, *et al.* A protein domain-based interactome network for C. elegans early embryogenesis. *Cell* **134**, 534-545 (2008).

55. Trokter M, Mucke N, Surrey T. Reconstitution of the human cytoplasmic dynein complex. *Proc Natl Acad Sci U S A* **109**, 20895-20900 (2012).

56. Yoder JH, Han M. Cytoplasmic dynein light intermediate chain is required for discrete aspects of mitosis in Caenorhabditis elegans. *Mol Biol Cell* **12**, 2921-2933 (2001).

57. Shivaraju M, Unruh JR, Slaughter BD, Mattingly M, Berman J, Gerton JL. Cell-cycle-coupled structural oscillation of centromeric nucleosomes in yeast. *Cell* **150**, 304-316 (2012).

58. Coupe P, Munz M, Manjon JV, Ruthazer ES, Collins DL. A CANDLE for a deeper in vivo insight. *Med Image Anal* **16**, 849-864 (2012).

59. Sage D, Neumann FR, Hediger F, Gasser SM, Unser M. Automatic tracking of individual fluorescence particles: application to the study of chromosome dynamics. *IEEE Trans Image Process* **14**, 1372-1383 (2005).

60. Jaqaman K, *et al.* Robust single-particle tracking in live-cell time-lapse sequences. *Nat Methods* **5**, 695-702 (2008).

61. Huet S, Karatekin E, Tran VS, Fanget I, Cribier S, Henry JP. Analysis of transient behavior in complex trajectories: application to secretory vesicle dynamics. *Biophysical journal* **91**, 3542-3559 (2006).

62. Monnier N, Guo SM, Mori M, He J, Lenart P, Bathe M. Bayesian approach to MSD-based analysis of particle motion in live cells. *Biophysical journal* **103**, 616-626 (2012).

63. Akhmanova A, Steinmetz MO. Control of microtubule organization and dynamics: two ends in the limelight. *Nat Rev Mol Cell Biol*, (2015).

64. Bieling P, *et al.* Reconstitution of a microtubule plus-end tracking system in vitro. *Nature* **450**, 1100-1105 (2007).

65. Duellberg C, Trokter M, Jha R, Sen I, Steinmetz MO, Surrey T. Reconstitution of a hierarchical +TIP interaction network controlling microtubule end tracking of dynein. *Nat Cell Biol*, (2014).

66. Skop AR, White JG. The dynactin complex is required for cleavage plane specification in early Caenorhabditis elegans embryos. *Curr Biol* **8**, 1110-1116 (1998).

67. Kamath RS, *et al.* Systematic functional analysis of the Caenorhabditis elegans genome using RNAi. *Nature* **421**, 231-237 (2003).

68. Segbert C, Barkus R, Powers J, Strome S, Saxton WM, Bossinger O. KLP-18, a Klp2 kinesin, is required for assembly of acentrosomal meiotic spindles in Caenorhabditis elegans. *Mol Biol Cell* **14**, 4458-4469 (2003).

69. Kozlowski C, Srayko M, Nedelec F. Cortical microtubule contacts position the spindle in C. elegans embryos. *Cell* **129**, 499-510 (2007).

70. O'Rourke SM, Christensen SN, Bowerman B. Caenorhabditis elegans EFA-6 limits microtubule growth at the cell cortex. *Nat Cell Biol* **12**, 1235-1241 (2010).

71. D'Alessandro M, *et al.* Amphiphysin 2 Orchestrates Nucleus Positioning and Shape by Linking the Nuclear Envelope to the Actin and Microtubule Cytoskeleton. *Dev Cell* **35**, 186-198 (2015).

72. Shaye DD, Greenwald I. OrthoList: a compendium of C. elegans genes with human orthologs. *PLoS One* **6**, e20085 (2011).

73. Varga V, Helenius J, Tanaka K, Hyman AA, Tanaka TU, Howard J. Yeast kinesin-8 depolymerizes microtubules in a length-dependent manner. *Nat Cell Biol* **8**, 957-962 (2006).

74. Varga V, Leduc C, Bormuth V, Diez S, Howard J. Kinesin-8 motors act cooperatively to mediate length-dependent microtubule depolymerization. *Cell* **138**, 1174-1183 (2009).

75. Von Smoluchowski M. Versuch einer mathematischen Theorie der Koagulationskinetik kolloidaler Lösungen. *Zeitschrift für physikalische Chemie* **92**, 129-168 (1917).

76. Fink J, *et al.* External forces control mitotic spindle positioning. *Nat Cell Biol* **13**, 771-778 (2011).

77. Thery M, *et al.* Anisotropy of cell adhesive microenvironment governs cell internal organization and orientation of polarity. *Proc Natl Acad Sci U S A* **103**, 19771-19776 (2006).

Movie legends

Movie S1. One-cell embryo carrying a randomly integrated DYCI-1::mcherry imaged during metaphase at the lower spindle plane (LSP). Acquisition was performed at 5Hz by spinning disk microscopy. The movie is accelerated to 3x real-time. No image processing was applied. Scale bar represents 10 μm.

Movie S2. One-cell embryo carrying a randomly integrated DYCI-1::mcherry imaged during anaphase at the lower spindle plane (LSP). Acquisition was performed at 5Hz by spinning disk microscopy. The movie is accelerated to 3x real-time. No image processing was applied. Scale bar represents 10 μm.

Movie S3. One-cell embryo carrying a randomly integrated DYCI-1::mcherry imaged during metaphase at the cortex. Acquisition was performed at 5Hz by spinning disk microscopy. The movie is accelerated to 3x real-time. No image processing was applied. Scale bar represents 10 μm.

Movie S4. One-cell embryo carrying a randomly integrated DYCI-1::mcherry and null mutation *dyci-1(tm4732)*, imaged during metaphase at the lower spindle plane (LSP). Acquisition was performed at 5Hz by spinning disk microscopy. The movie is accelerated to 3x real-time. No image processing was applied. Scale bar represents 10 μm.

Movie S5. One-cell embryo carrying a randomly integrated DYCI-1::mcherry and null mutation *dyci-1(tm4732)*, imaged during metaphase at the cortex. Acquisition was performed at 5Hz by spinning disk microscopy. The movie is accelerated to 3x real-time. No image processing was applied. Scale bar represents 10 μm.

Movie S6. Membrane invaginations pulled from cytoplasmic membrane towards cell center, in an embryo doubly labeled by DYCI-1::mcherry (left) and PLCδ1-PH::GFP (center) upon partial *nmy-2(RNAi)*. Right panel shows the overlay of left and middle panels. Embryo was imaged at 2.5Hz by spinning disk. The movie is 7x real-time. Both channels are filtered by CANDLE algorithm for better visibility. Scale bar represents 10 μm.

Movie S7. Simulated fluorescence microscopy stream depicted diffusive particles with an exponential distributed lifetime, with time constant of 10 s. Frame rate is 5 Hz. Signal to noise ratio was 5. The movie is accelerated to 3x real-time. Scale bar represents 10 μm.

Movie S8. Simulated fluorescence microscopy stream depicted particles with direct motion with an exponential distributed lifetime, with time constant of 10 s.

Frame rate is 5 Hz. Signal to noise ratio was 5. The movie is accelerated to 3x real-time. Scale bar represents 10 μm.

Movie S9. Embryo labeled with DYCI-1::mcherry (red) and α-tubulin::YFP (green), acquired at LSP. The inset is a zoom in the region delineated by the white square. The movie is filtered by CANDLE and LoG filter (see SI text) and accelerated to 7x real-time. Scale bar represents 10 μm.

Movie S10. Embryo labeled with DYCI-1::mcherry (red) and EBP-2::GFP (green), acquired at LSP. The movie is filtered by CANDLE and LoG filter (see SI text) and accelerated to 7x real-time. Scale bar represents 10 μm.

Movie S11. Invagination at the cortex of an embryo acquired at 2.5 frame/s in doubly labeled strain upon *nmy-2(RNAi)*. Green channel, PLCδ1-PH::GFP and red channel DYCI-1::mcherry. The movie corresponds to stills in fig. S3C.

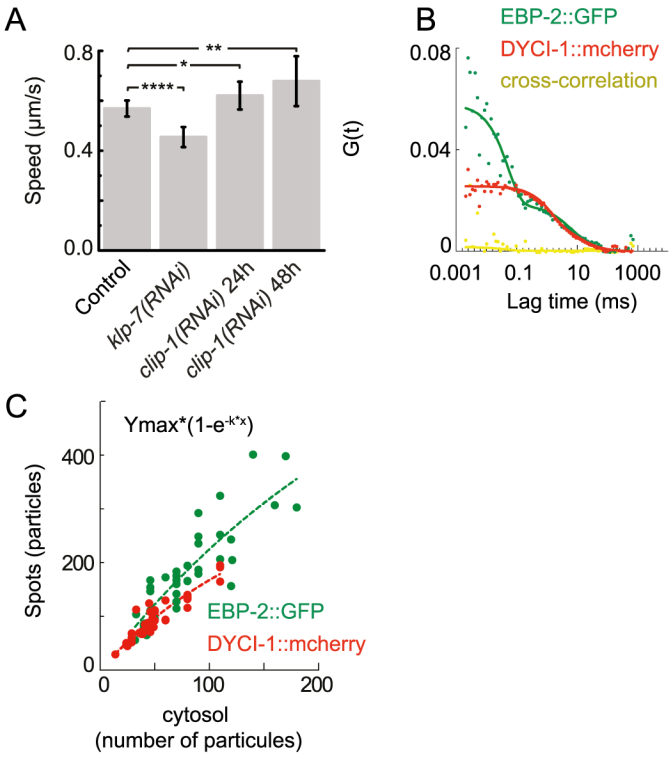

Figure S1: dynamics of DYCI-1::mcherry and EBP-2 in cytoplasm and at microtubule plus-ends.

(**A**) Velocity of DYCI::mcherry spots, in the lower spindle plane for four conditions modulating microtubule dynamics. Data come from 7 embryos and 1500 trajectories per condition. Error bars are standard errors. (**B**) Autocorrelation of DYCI-1::mcherry (red dot) and EBP-2::GFP (green dot) measured by dual color FCS. Experimental curves were fitted to a triplet state model for one fluorescent species (plain line, same color code, see SI text). Cross-correlation curve (dot) and its fitting by the same model (plain line) are in yellow. (**C**) Number of particles in spots compared to the local density of particles in the cytoplasm as measured by FCS (see SI text and Fig. 3C for a typical trace), for DYCI-1::mcherry (red) and EBP-2::GFP (green). The dashed lines represent the fit with an exponential growth of the experimental curves: equation reads $P_{MT-tip} = Y_{max}\left(1 - e^{-kP_{cyto}}\right)$. We obtained the following fitted values: $Y_{max}^{DYCI-1} = 354$; $k^{DYCI-1} = 0.006$ and $Y_{max}^{EBP-2} = 760$; $k^{EBP-2} = 0.003$ (N=8 embryos, 43 spots).

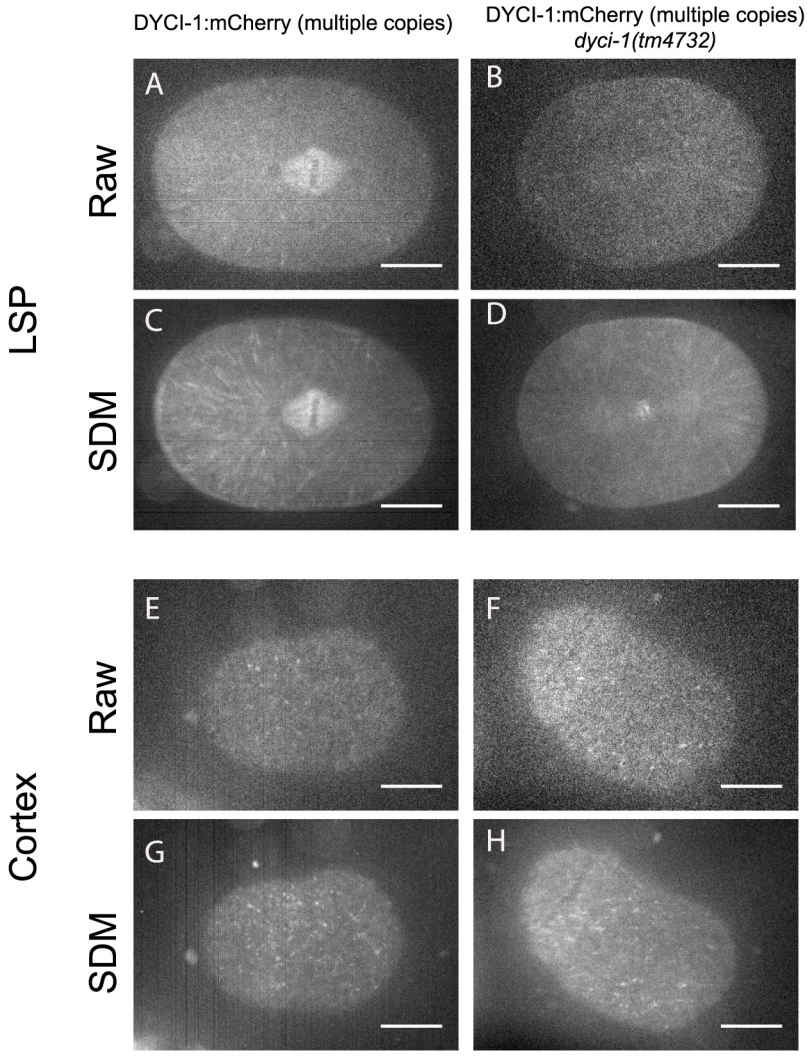

Figure S2: micrographs of DYCI-1::mcherry in lower spindle plane and at the cortex
Micrographs of randomly integrated DYCI-1::mcherry, (ACEG) in normal condition and (BDFH) where endogenous protein was depleted through the null mutation *dyci-1(tm4732)*. (AB,EF) are raw pictures and (CD,GH) are standard deviation maps (SDM, see SI material and methods) obtained over 125 pictures acquired at 5 frames/s. Embryos were imaged in the lower spindle plane (LSP) (A-D) and at the cortex (E-H) by spinning disk microscopy. Scale bars are 10 µm.

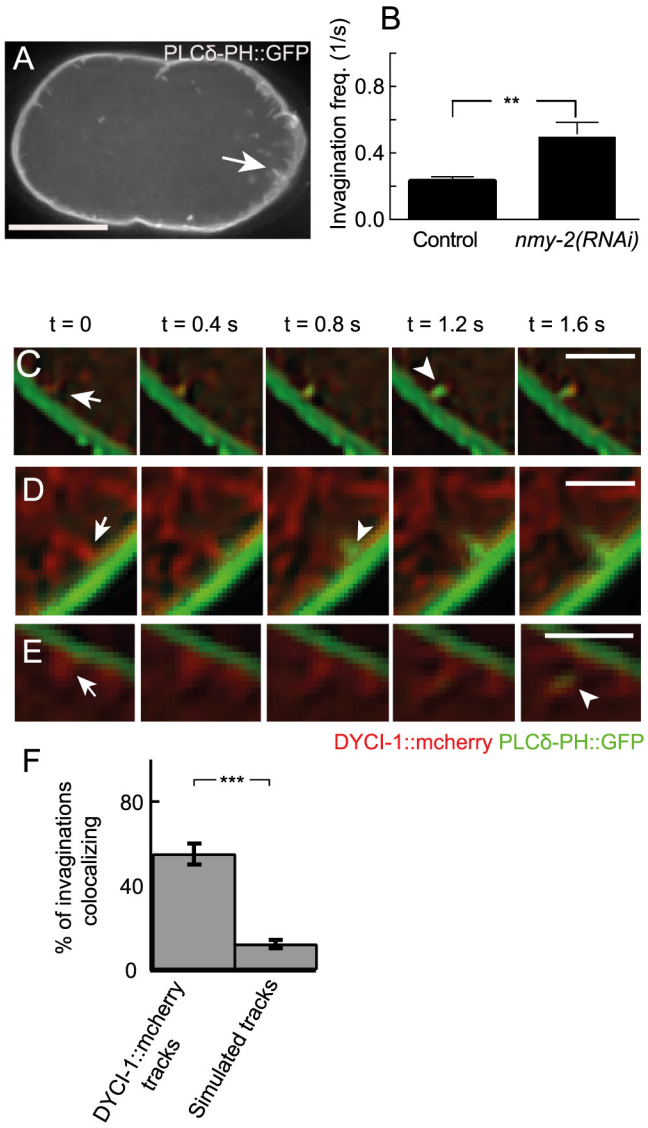

Figure S3: dynein spots co-localize with membranes invaginations in DYCI-1::mcherry PLCδ-PH::GFP strain.

(**A**) Maximum intensity projection over 30 frames acquired at 2.5 frames/s of a doubly labeled DYCI-1::mcherry ; PLCδ-PH::GFP strain. Scale bar is 10 µm. A white arrow shows an exemplar invagination. (**B**) Invagination frequency in control and weakened actin-myosin cortex by *nmy-2(RNAi)* conditions. Error bars are standard deviations, N= 11 embryos (control) and N=20 embryos for *nmy-2(RNAi*). Frequencies are significantly different $p<0.001$ using Mann-Whitney/Wilcoxon test. (**C-E**) Three examples of invagination image sequence acquired during 15 frames at 2.5 frame/s in doubly labeled strain upon *nmy-2(RNAi)*. Green channel, PLCδ1-PH::GFP and red channel DYCI-1::mcherry. Membrane invagination (arrowheads) started after dynein appeared at the cortex (arrows). Scale bars are 2 µm. (**F**) Fraction in percent of invaginations colocalizing with DYCI-1::mcherry tracks (left, N=18 embryos, 139 invaginations) compared to colocalizing with simulated random trajectories in equal number (right, SI text § 1.2.2). Statistical significance was indicated by stars using Mann-Whitney/Wilcoxon test. Error bars are s.e.m.

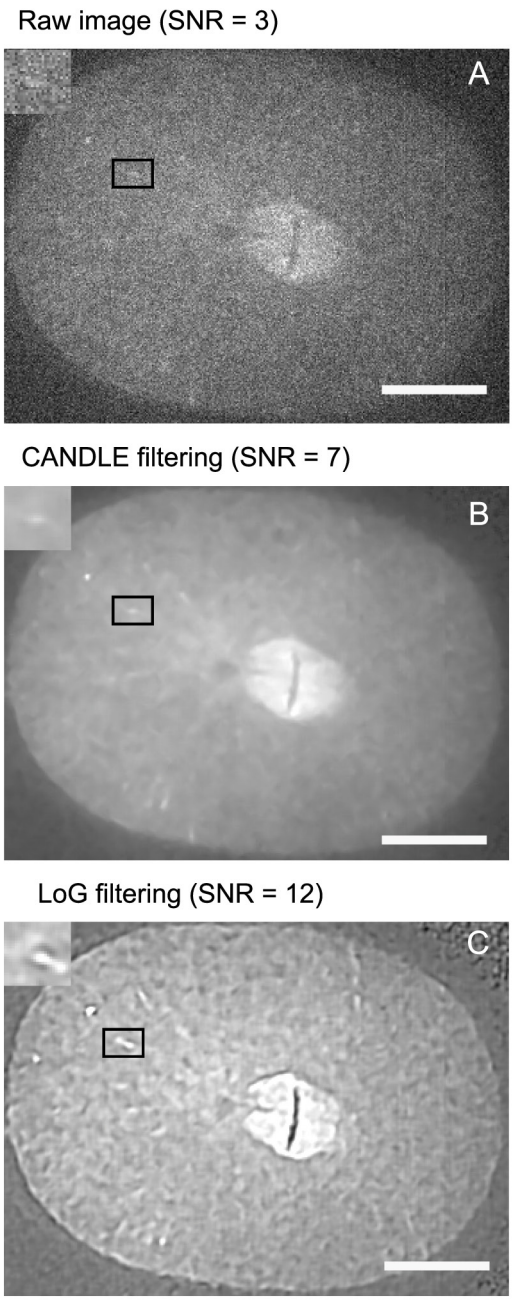

Figure S4: a typical DYCI-1::mcherry micrograph analyzed through our *tracking pipeline*. One-cell embryo during metaphase acquired with a 0.2 s exposure. Insets are magnified views of the region delineated by the black rectangle and highlighting a spot. Scale bars are 10 μm. Images obtained at each step of preprocessing: (**A**) Raw picture; (**B**) denoised image by CANDLE filter; (**C**) then after 2-D LoG filter (see SI text).

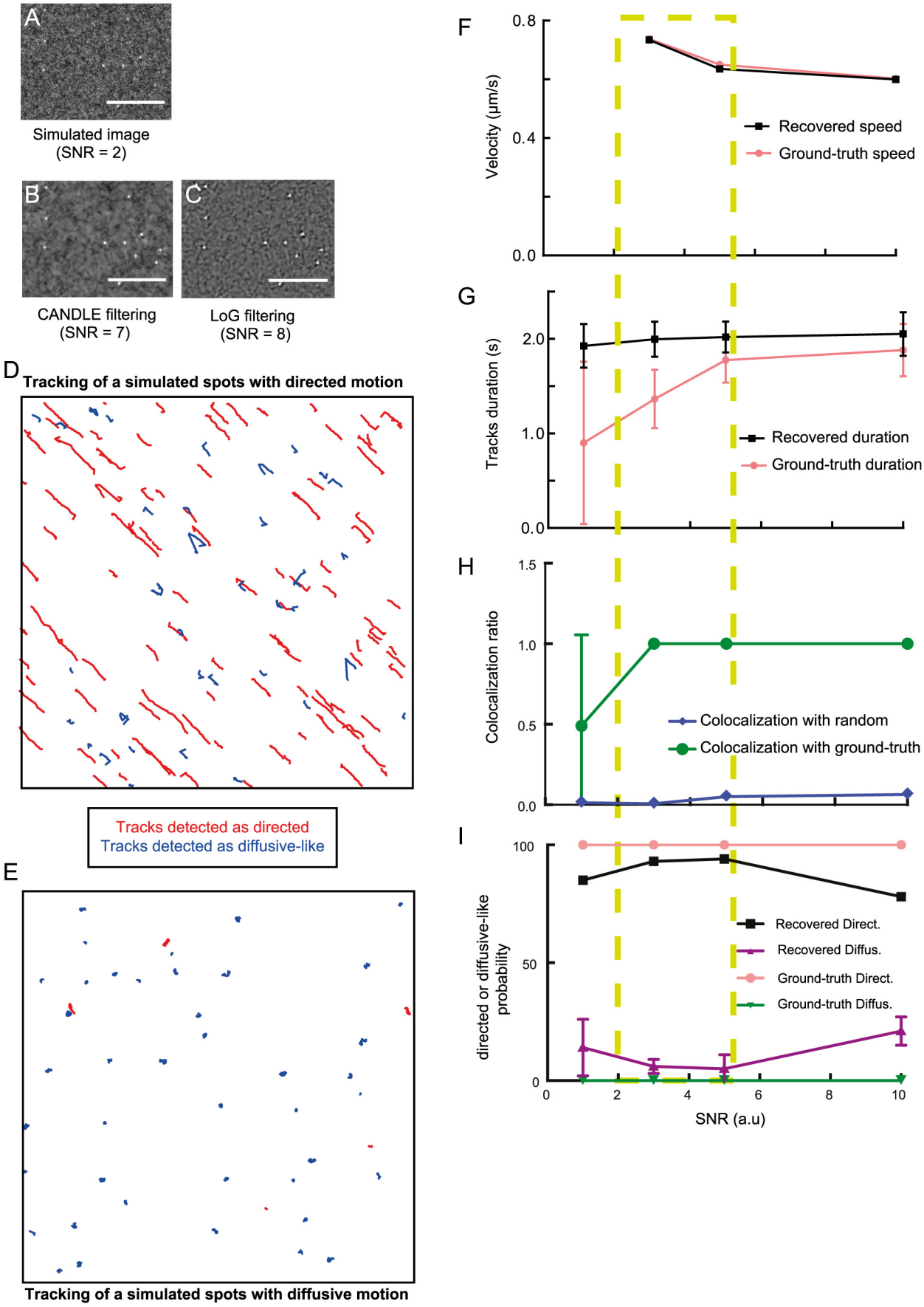

Figure S5 (legend on next page)

Figure S5: the tracking pipeline is validated through fabricated images mimicking experimental ones.

Fabricated image with known spots dynamics and mimicking experimental ones (see SI text) analyzed with our pipeline. Scale bars are 10 μm. Images obtained at each step of preprocessing: (**A**) Raw picture; (**B**) denoised image by CANDLE filter; (**C**) then after 2-D LoG filter (see SI). (DE) Typical tracking of two simulated movies where spots displayed (**D**) directed and (**E**) diffusive motions. Classification of the tracks recovered by our analysis pipeline was color coded: in red for directed motion and in blue for diffusive-like. (FG, I) The yellow-green dashed rectangle highlights the SNRs values corresponding to the ones observed experimentally. We compared (**F**) tracks average speed and (**G**) tracks average duration set by the simulation (ground-truth, red dots) and the ones recovered by our analysis (black squares) for directed tracks. (**H**) We also tested the colocalization of the tracks (green dots) compared to random colocalization (blue diamonds). (**I**) We eventually challenged the classification by computing the recovered ratio of tracks classified as directed (black squares) and diffusive-like (purple upward triangles) in percent, to be compared to values prescribed to the simulation for directed (red dots) and diffusive-like tracks (downward green triangles). Error bars are s.e.m.

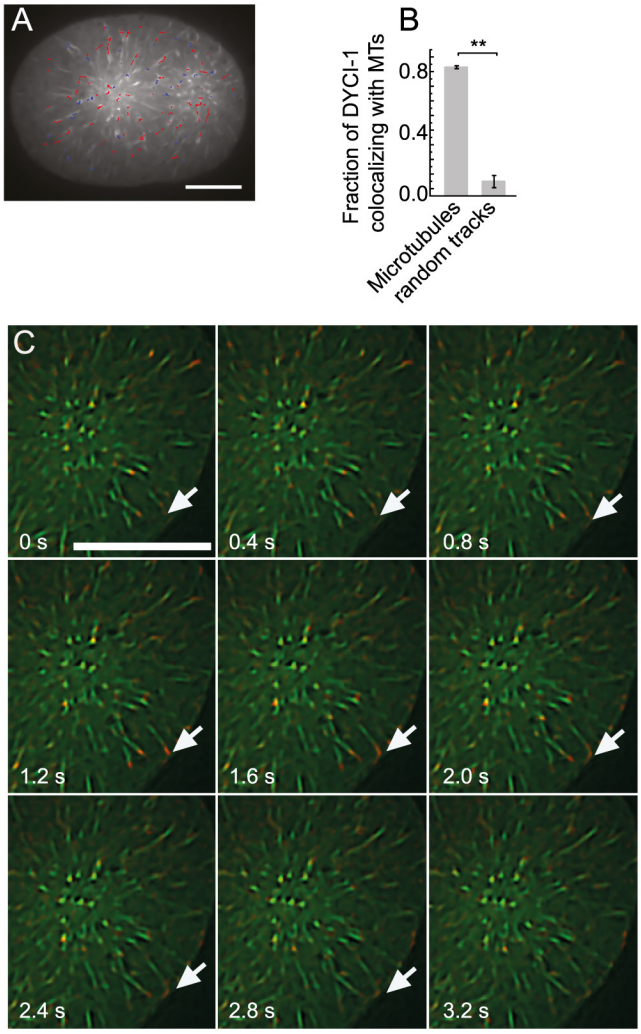

Figure S6: directed tracks of DYCI-1::mcherry spots colocalized with microtubule.
(**A**) DYCI-1::mcherry tracks, classified between directed to the cell periphery (red), to the center (orange) and diffusive-like (blue), superimposed to the maximum intensity projection of microtubules (α-TUBULIN::GFP) computed from a 10 frames dual color stack acquired at 2.5 frames/s. Scale bar is 10 µm. (**B**) Fraction of DYCI-1::mcherry spots colocalizing with microtubule compared to colocalizing with simulated random tracks (see SI material and methods) (N=5 embryos, 9 stacks, 200 tracks). Statistical significance was indicated by stars using Mann-Whitney/Wilcoxon test. Error bars are standard errors. (**C**) Sequence of micrographs, acquired each 0.4 s, displaying DYCI-1::mcherry (red) and α-tubulin::YFP (green). Arrows show a microtubule tip where DYCI-1::mcherry is accumulated. Scale bar is 5 µm.

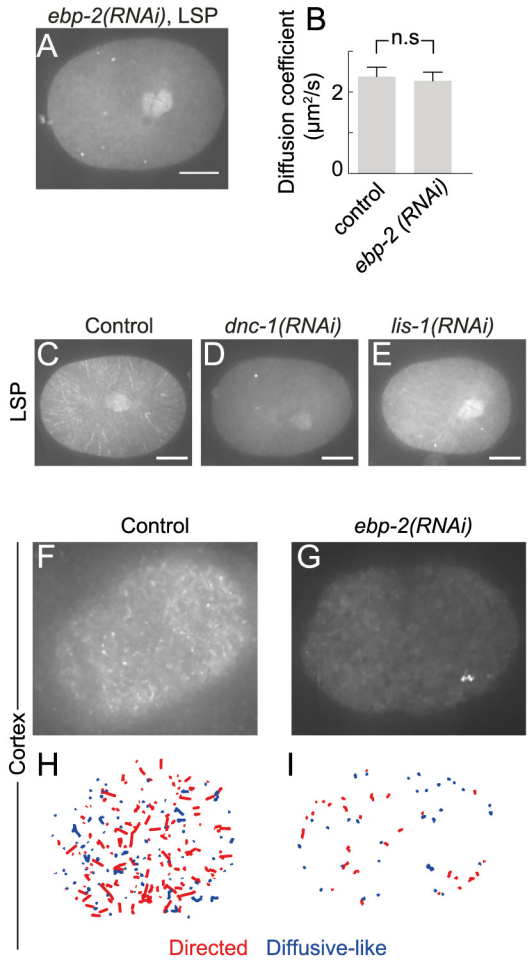

Figure S7: DYCI-1::mcherry directed motion in LSP is dependent on EBP-2, dynactin and LIS-1. Cortex targeting depends on EBP-2.
(**A**) Maximum intensity projection computed from a 100 frames (5 frames/s) DYCI-1::mcherry movie upon partial *ebp-2(RNAi*) (feeding, 20h). (**B**) Diffusion coefficients measured by FCS in the cytoplasm for the doubly labeled DYCI-1::mcherry EBP-2::GFP strain, upon *ebp-2(RNAi)* (N=5 embryos, 3 FCS spots per embryo). Error bars are s.e.m. (C-E) Maximum Intensity Projection computed from a 100 frames (5 frames/s) movie of DYCI-1::mcherry. (**C**) non-treated, (**D**) upon *dnc-1(RNAi)* and (**E**) *lis-1(RNAi)*. Scale bars are 10 μm. Typical (**F**) control and (**G**) *ebp-2(RNAi)* treated DYCI-1::mcherry embryos imaged at the cortex after CANDLE preprocessing to enhance visibility (SI text §1.3.1) and (**HI**) tracking in the same conditions, respectively.

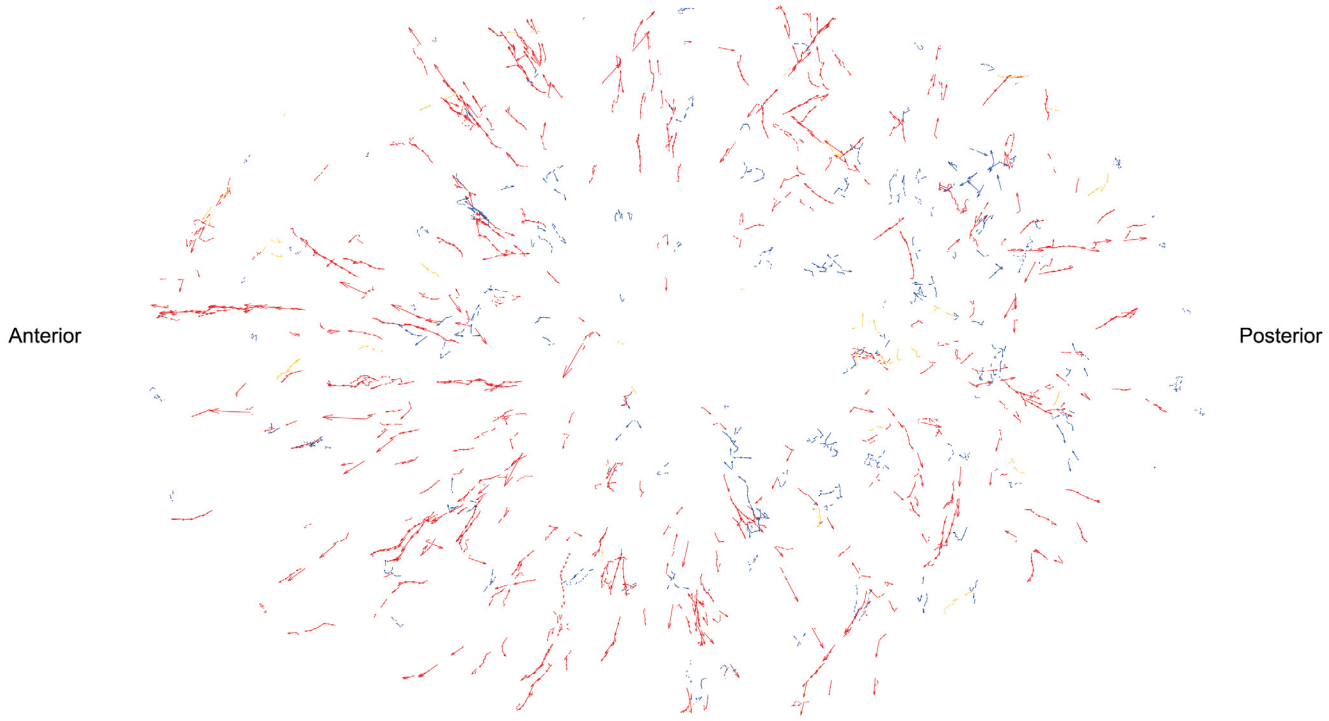

Figure S8: DYCI-1::mcherry velocity map of spots acquired at the LSP.
Velocity map obtained in LSP for the same embryo as the one represented in fig 1A. Velocities are depicted by small arrows of length proportional to instantaneous speed. Trajectories were classified between directed to the cell periphery (red), to the center (orange) and diffusive-like (blue). Inset, zoom into a region highlighting radial alignment of the directed tracks.

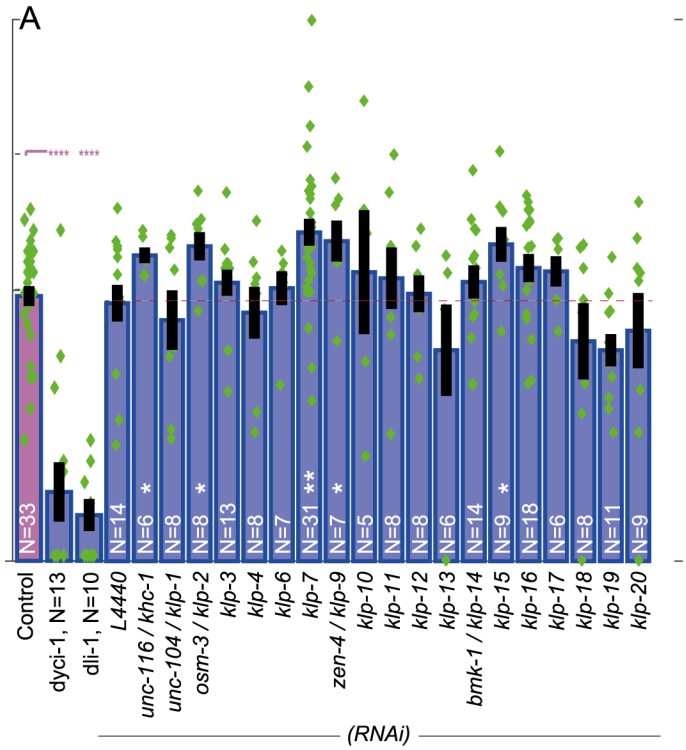

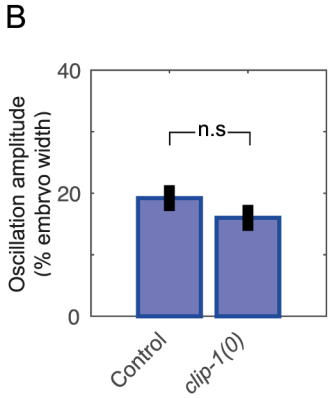

Figure S9: anaphase posterior centrosome oscillations upon kinesins depletion.
(**A**) Anaphase posterior centrosome oscillations maximum amplitude in % of embryo width obtained upon partial RNAi of each kinesin and DYCI-1 or DLI-1 partial depletions for reference. Green diamonds correspond to raw data. Horizontal dashed line indicates the amplitude for non-treated embryos. White stars indicate significant differences with respect to *L4440(RNAi)* and pink stars with respect to control. (**B**) Anaphase posterior centrosome oscillations maximum amplitude in % of embryo width in N=10 control γTUB::GFP embryos and N=10 embryos crossed with null mutant *clip-1(gk470)*. Black error bars correspond to s.e.m

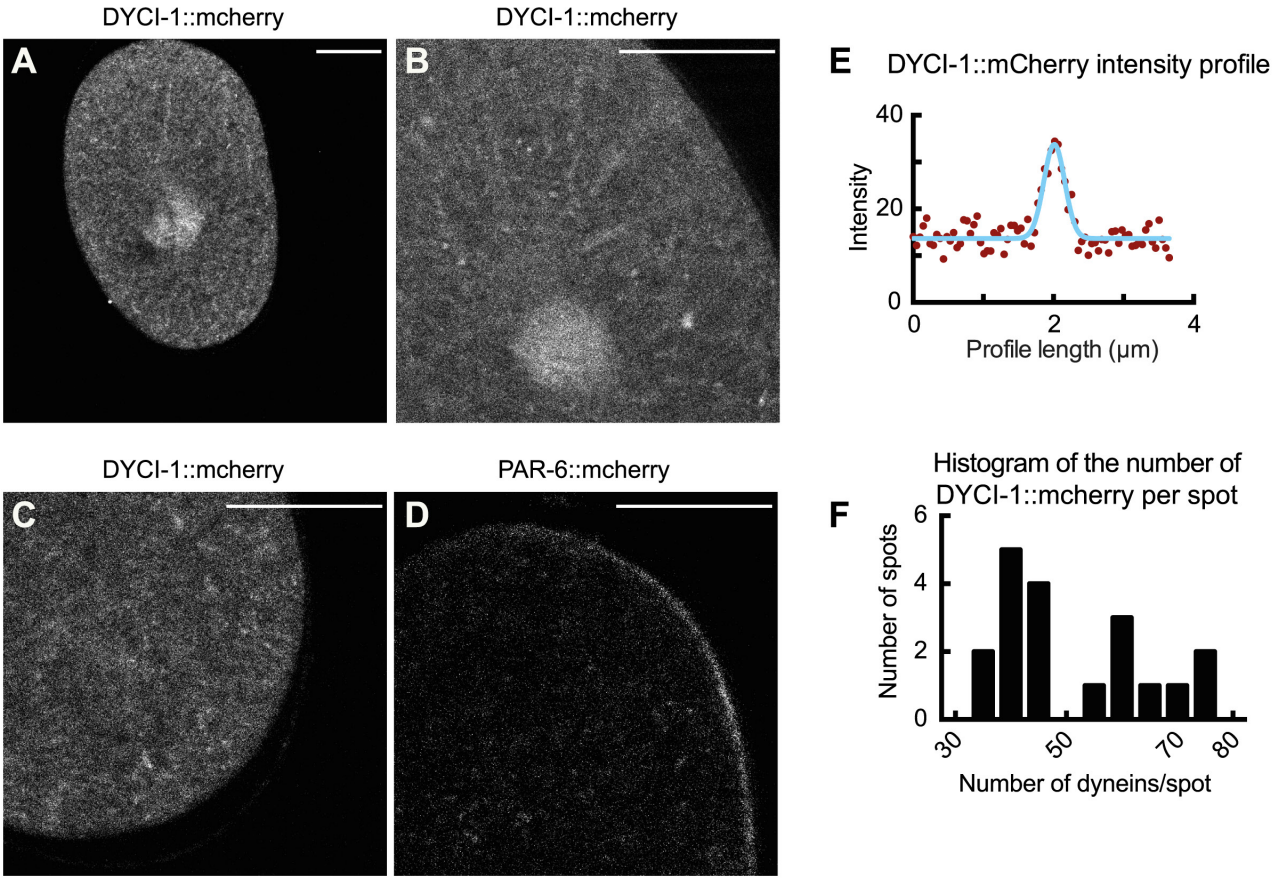

Figure S10: counting the number of dynein per spots at microtubule plus-ends through image intensity.
Typical micrographs of (**A**, **B** and **C**) DYCI-1::mcherry used to measure spots intensity profile and (**D**) PAR-6::mcherry used to calibrate intensity into a number of mcherry dyes. Scale bars are 10 µm. (**E**) Exemplar fit of a DYCI-1::mcherry spot intensity profile by a Gaussian with background. (**F**) Histogram of intensities of the spots measured as the amplitude of the fitted Gaussian, background subtracted.

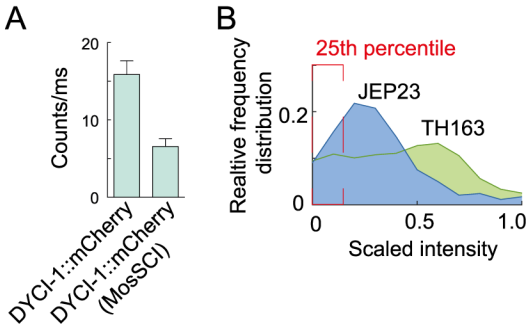

Figure S11: DYCI-1::mcherry level of expression and detection threshold.
(**A**) Average value of intensity (counts per millisecond) in the cytoplasm obtained by FCS for the randomly integrated DYCI-1::mcherry (TH163) N=6 embryos, 38 spots and the one carrying exactly two copies of DYCI-1::mcherry (JEP23) N=10 embryos, 52 spots. Error bars are standard error of the mean (**B**) Intensity histogram from tracked spots in the strain carrying exactly two copies of DYCI-1::mcherry (JEP23, blue area, N=6 embryos, 52 spots) and the randomly integrated DYCI-1::mcherry strain (TH163, green area, N=6 embryos, 59 spots). The intensity values were scaled from 0 to 1 for plotting, where 0 is the minimum value and 1 is the maximum. Dashed red line represents the 25 percentile for JEP23.

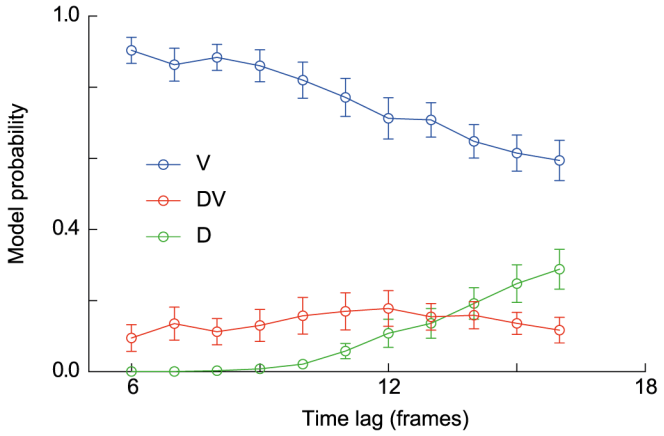

Figure S12: exemplar probabilities of concurrent models in Bayesian classification analysis (BCA) upon varying the mean square displacement (MSA) time lag.
Mean value of the model probability estimated for 3 models (V, DV, D) by BCA classification pipeline (see SI text) and computed over N=31 embryos. The average values are represented *versus* the different lag times used to calculate the mean square displacement (see SI). The error bar represents the standard error of the mean between embryos for each lag time. The graph corresponds to the case of directed tracks in the LSP in control embryos.

Supplementary text and materials and methods to Dynamics of dynein at microtubule plus-ends and the cortex during the division of the *C. elegans* zygote

Ruddi Rodriguez Garcia[1,2,3, *], Laurent Chesneau[1,2,*], Sylvain Pastezeur[1,2], Julien Roul[1,2,4], Marc Tramier[1,2] and Jacques Pécréaux[1,2,#]

1. CNRS, UMR6290, Institute of Genetics and Development of Rennes (IGDR), F-35043 Rennes, France

2. University Rennes 1, UEB, SFR Biosit, School of medicine, F-35043 Rennes, France

3. Present address: Cell Biology, Faculty of Science, Utrecht University, Padualaan 8, 3584 CH Utrecht, The Netherlands.

4. Present address: LAAS - Laboratoire d'analyse et d'architecture des systèmes, 7, avenue du Colonel Roche BP 54200, 31031 Toulouse cedex 4, France.

1. SUPPLEMENTARY TEXT

1. Supplementary text 2

1.1 DYCI-1::mCherry is a bona fide reporter of dynein dynamics. 4

1.1.1 DYCI-1::mCherry is a functional transgene. 4

1.1.2 Rescue of null recessive embryonic lethal mutation *dyci-1(tm4732)* by DYCI-1::mcherry transgene. 4

1.1.3 DYCI-1::mCherry fluorescent spots are not artifacts of the overexpression. 5

1.1.4 Measuring cytoplasmic concentration by FCS 5

1.1.5 Measuring binding rate to the microtubule plus-ends. 6

1.1.6 Tube assay in doubly membrane and dynein labeled strain. 6

1.1.7 Estimating threshold detection. 7

1.1.8 DYCI-1::mcherry remains associated to the dynein complex 7

1.2 Characterizing DYCI-1::mCherry dynamics. 8

1.2.1 Counting molecules bound to the microtubule plus-ends through two independent approaches 8

1.2.2 Colocalizing DYCI-1::mCherry and astral microtubules. 9

1.2.3 Characterizing dynein unbinding dynamics at microtubule plus-end and Modulating microtubule growth rate. 9

1.2.4 Measurement of cortical pulling forces upon depletion of kinesins. 10

1.2.5 Measuring dynein residency time at the cortex. 10

1.2.6 Estimating the rate of dynein reaching the cortex by 3D diffusion. 10

1.3 Image processing pipeline to characterize dynein dynamics 11

1.3.1 Preprocessing of the images 11

1.3.2 Automated tracking of DYCI-1::mCherry fluorescent spots. 11

1.3.3 Classification of the tracks 12

1.3.4 Analysing simulated microscopy images to validate the image processing and data analysis pipeline. 13

2. Materials and Methods 15

2.1 Culturing C. elegans 15

2.2 C. elegans strains used 15

2.3 Gene silencing by RNA interference 15
2.4 Live Imaging 16
2.5 FCS and FCCS measurements 17
2.6 Image processing 17
2.7 Statistics 17
2.8 Code and data availability 18
3. References 18

1.1 DYCI-1::MCHERRY IS A BONA FIDE REPORTER OF DYNEIN DYNAMICS.

In this paper, we set to offer a detailed view of the dynamics of dynein at microtubule plus-ends, firstly, to clarify how it is efficiently targeted to the cell periphery and whether it is a transport mechanism and secondly, to measure the dynamics of dynein at the cell cortex. To do so, we used a fluorescent reporter of dynein light chain (Fig 1, Movies S1-3). We then applied tracking and detailed quantification (Fig. 2). To fully take advantage of this quantification, it is crucial to ensure that the fluorescent transgene reports faithfully all localization of dynein, without artifact due to altered expression level or other causes on the one hand, and on the other hand, that the labeled dynein can perform similarly to the endogenous dynein, in particular contributing to pulling force generation.

1.1.1 DYCI-1::MCHERRY IS A FUNCTIONAL TRANSGENE

To investigate the *in vivo* dynamics of dynein targeting to the cortex and its residency there, we used the strain TH163, carrying a randomly integrated transgene encoding the fluorescently labeled dynein sub-unit DYCI-1::mcherry, flanked with the endogenous regulatory sequences and produced in the framework of the transgeneOme project (Sarov et al., 2012; Sarov et al., 2006). We observed variability in the expression assessed through fluorescence intensity in the one-cell embryo. Embryos did not show significant phenotype or lethality compared to wild type (N2, N>30). In contrast to mammalian cells, DYCI-1 is the sole dynein intermediate chain needed in early embryo while its paralog, identified through panther algorithm (Mi et al., 2010; Mi et al., 2013), C27F2.1, is dispensable (Kamath et al., 2003; Sonnichsen et al., 2005). Therefore, we can expect this transgene to report all dynein complexes.

1.1.2 RESCUE OF NULL RECESSIVE EMBRYONIC LETHAL MUTATION *DYCI-1(TM4732)* BY DYCI-1::MCHERRY TRANSGENE.

We first aimed to validate that the transgene is functional by rescuing the null and recessive lethal mutation *dyci-1(tm4732)* with the randomly integrated transgene. To do so, we first crossed the strain carrying DYCI-1 null mutation *tm4732* with the strain VC2542 carrying a balancer featuring a pharynx/gut GFP marker and the homozygous lethal re-arrangement nT1[qIs51] (and two wild-type copy of *dyci-1*), producing strain JEP9. We then crossed this strain twice with randomly integrated DYCI-1::mcherry TH163 strain, to obtain JEP40. JEP40 contained no endogenous copy of *dyci-1* gene, but only mcherry labeled ones. It displayed reduced embryonic lethality and some dumpy/unc phenotype.

We noticed a variability in fluorescence level in the randomly integrated DYCI-1::mcherry, therefore, we wondered about the level of expression. We designed the strain JEP23 together with the "Biology of Caenorhabditis elegans" facility (UMS3421, Lyon, France), carrying exactly two copies of the transgene using MosSCI (Boulin and Bessereau, 2007; Robert and Bessereau, 2007). For this purpose, dyci-1::mcherry sequence (3035 nucleotides before dyci-1 5'UTR to end of 3'UTR) was amplified from TH163 genomic DNA, cloned into Afl II/Bgl II site of pCFJ352 plasmid and bombarded into EG6701 strain, generating JEP23 strain. Integration on ttTi4348 Mos site was verified by sequencing. We crossed twice the JEP23 strain with null mutation tm4732 JEP9 strain to get the strain JEP30.

Worms homozygous for dyci-1::mcherry insertion and heterozygous for null mutation *dyci-1(tm4732)* produced viable homozygote null mutant progeny, which in turn produced progeny showing embryonic lethality. We further investigated the second generation: in worms homozygous for *tm4732* mutation and carrying 2 copies of DYCI-1::mcherry, we rarely observed more than 2 pronuclei (2/11embryos). In embryos with two *pronuclei*, they met in 6/9 embryos and in these, spindle was often ill-formed (5/6) but usually (partially) migrated to the cell center, oriented along the antero-posterior axis (4/6) prior to cytokinesis onset. Furrow initial ingression was well positioned (4/6). Overall, it phenocopied a mild RNAi depletion of *dyci-1* observed between 12 and 19h after transfer on feeding plate. We concluded that the products of the DYCI-1::mcherry transgene can fulfill the role of DYCI-1.

1.1.3 DYCI-1::MCHERRY FLUORESCENT SPOTS ARE NOT ARTIFACTS OF THE OVEREXPRESSION.

Because the number of DYCI-1::mcherry transgene copies is not constrained in the strain where it was randomly integrated, we reasoned that the spots of DYCI-1 could be non-physiological, due to over-expression. We imaged the strains devoid of endogenous copies of dyci-1 (Fig S2). In the case of randomly integrated DYCI-1::mcherry (Fig. S2 BD, FH, Movie S4-5) like in the case of integrating exactly two copies, we successfully detected spots in LSP and at the cortex. However, with exactly two copies, spots were much fainter than with randomly integrated DYCI-1::mcherry transgene precluding quantification. We concluded that the observed spots in randomly integrated DYCI-1::mcherry strain carrying endogenous copies (further referred simply as DYCI-1::mcherry) are not artefactual and are representative of dynein dynamics.

1.1.4 MEASURING CYTOPLASMIC CONCENTRATION BY FCS

We then asked whether the observed spots could be passive aggregates. We addressed this question by investigating their dynamics, in particular in the cytoplasm (LSP) by FCS: we investigated the association kinetics of the spots from cytoplasmic fraction of DYCI-1::mcherry. We first measured the cytoplasmic concentration by FCS. In further details, FCS traces (Fig. 3C e.g.) were analyzed using Symphotime (PicoQuant). We fitted the autocorrelation function $G(\tau)$ using triplet state model for one fluorescent specie (Widengren et al., 1994) as:

$$G(\tau) = G(0)\left[1 - T + Te^{\left(-\frac{t}{\tau_T}\right)}\right]\left(1 + \frac{t}{\tau}\right)^{-1}\left(1 + \frac{t}{\tau\kappa^2}\right)^{-1/2} \quad \text{(S1)}$$

where t is the lag time in ms, T is the fraction of triplet decay, τ_T is the lifetime of the triplet state in ms, τ is the diffusion time of the fluorescent specie in ms and κ is the length to diameter ratio of the focal volume set to 4. Then, we calculated the concentration in the cytoplasm as $C = \frac{1/G(0)}{V_{eff}N_A}$ where V_{eff} is the effective excitation volume and N_A is the Avogadro number. We measured 32 ± 11 particles in the focal volume, estimated to 0.3 fl, leading to an estimated concentration of 177 ± 60 nM.

1.1.5 MEASURING BINDING RATE TO THE MICROTUBULE PLUS-ENDS.

To analyze the dynamics of dynein spots and estimate the binding rate of dynein to a microtubule plus-end, we followed (Dragestein, 2008) and fitted the number of units bound at the plus-end versus the concentration in the cytosol with equation:

$$P_{MT-tip} = Y_{max}\left(1 - e^{-kP_{cytosol}}\right) \qquad \text{(S2)}$$

where P_{MT-tip} is the number of units at the plus-end of the microtubule, $P_{cytosol}$ the concentration in cytoplasm within FCS focal volume, k the binding rate and Y_{max} the maximum number of units at the plus-end. We measured the cytoplasmic concentration as detailed above. The number of particles in the peak was obtained by multiplying the ratio of peak to basal intensity in the FCS trace (e.g. Fig. 3C) with the corresponding cytoplasmic concentration. We analyzed 43 spots in 8 embryos of the double labeled strain expressing DYCI-1::mcherry and EBP-2::GFP and, for each channel, fitted the respective measurements with equation S2. DYCI-1::mcherry and EBP-2::GFP displayed similar dynamics with, in particular, similar binding rate $k^{DYCI-1} = 0.006$ and $k^{EBP-2} = 0.003$ (Fig. S1C). By Fluorescence Correlation Cross Spectroscopy (FCCS), we showed that these two molecules are not associated in the cytoplasm (Fig. S1B). We concluded that aggregates are not passive but biologically relevant.

1.1.6 TUBE ASSAY IN DOUBLY MEMBRANE AND DYNEIN LABELED STRAIN.

On the functional side, we were interested in dynein contribution to cortical pulling forces generation (Nguyen-Ngoc et al., 2007; Pecreaux et al., 2006a). We tested whether cortical DYCI-1::mcherry is involved in pulling forces generation using the previously established "tube assay"(Redemann et al., 2010). In that experiment, the position of the cortical forces generators is revealed through their pulling of cytoplasmic membrane tubes towards the centrosomes, once the actin-myosin cortex has been weakened. Partial *nmy-2(RNAi)* was used to weaken enough the cortex while preserving polarity. To do so, we generated a new strain (JEP20) expressing both DYCI-1::mcherry and the PH-domain of the phospholipase fused to GFP, PLCδ1-PH::GFP, to visualize the plasma membrane (Fig. S3A, Movie S6). We measured that 55 ± 5 % of the invaginations displayed a DYCI-1::mcherry labeling upon *nmy-2(RNAi)* (N=18 embryos, 139 invaginations, main text, Fig. S3C-E, Movie S11). Interestingly and in contrast with this previous work, we observed 22 ± 13 invaginations (N=20 embryos) without treatment with an occurrence frequency of 0.51 ± 0.07 s^{-1} during anaphase compared to 9 ± 7 invaginations with a frequency of 0.23 ± 0.03 s^{-1} in control without DYCI-1::mcherry (N=11 embryos, Fig. S3B). This count of invaginations in DYCI-1::mcherry strain is also larger than previously reported for non-treated embryos. More importantly, we also observed that 42 ± 7 % of membrane invaginations are dynein decorated in non-treated embryos (N=8 embryos, 84 invaginations). In conclusion, because of the good colocalizing of dynein and invaginations upon *nmy-2(RNAi)*, we suggest that labeled dynein can be involved in cortical pulling force generation.

It is likely that the half of invaginations not visibly tagged contains an amount of DYCI-1::mcherry below our detection limit. Invagination physics was studied *in vitro* and theory suggested that forces in the tens of pN could be sufficient to pull one (Dernyi et al., 2002; Leduc et al., 2004). Stall force for a dynein is estimated at about 6 pN (Howard, 2001). We estimated (see § 1.1.7 just below) that our detection threshold is 26 dyneins. Such a number of dyneins is producing largely more forces than needed if all engaged. It is therefore expected that some invaginations displayed a number of dyneins lower than the threshold. We concluded that the strain DYCI-1::mcherry reports correctly the dynein relevant to cortical force generation and is therefore appropriate to investigate its localization and dynamics.

1.1.7 ESTIMATING THRESHOLD DETECTION.

We reasoned that the large cytoplasmic concentration of dynein could limit our ability to detect spots with a low number of units. We computed the detection threshold by considering the microtubules plus-ends spots intensities in the strain with exactly two copies of DYCI-1::mcherry integrated by MosSCI (JEP23) since it is close to our detection limit (see cytoplasmic intensities in Fig. S11A). We assumed that the intensities of spots distribute normally above a constant background. We fitted gaussian with an added constant for JEP23 strain, in N=6 embryos (41 spots) and for the DYCI-1::mcherry strain (N=6 embryos, 52 spots) to determine the background levels. We next subtracted this constant to the distribution and computed the 25th-percentile. (Fig. S11B). This value is however in intensity.

To convert this value in particles number, we considered that the average of the background subtracted intensities distribution for doubly labeled DYCI-1::mcherry EBP-2::GFP strain corresponds is the same as for JEP23 strain above, i.e. equal $P_{MT\text{-}tip}$ particles estimated above (see also §1.1.5). Proportionally, we obtained the corresponding number of particles for the 25th-percentile of JEP23 intensities distribution. We found a threshold of 26 ± 4 particles.

1.1.8 DYCI-1::MCHERRY REMAINS ASSOCIATED TO THE DYNEIN COMPLEX

To gain further confidence, we sought indications that DYCI-1 remained associated to the complex. To do so, we used fluorescent correlation spectroscopy (FCS) to estimate the size of labeled "particles" in the cytoplasm through measuring their diffusion coefficient. We found $D = 2.6 \pm 0.7\ \mu m^2 s^{-1}$ (N=9 embryos, 38 spots) compared to $D_{par-6} = 15 \pm 3\ \mu m^2 s^{-1}$ (N=4 embryos, 12 spots) for PAR-6::mcherry, used as a control. To interpret these results, we inferred viscosity of the cytoplasm from this PAR-6::mcherry control and computed an hydrodynamics radius for DYCI-1::mcherry associated complex using Stokes–Einstein–Sutherland equation assuming that PAR-6 is globular-shaped from what is known about its domains (Garrard et al., 2003; Hirano et al., 2005), as identified by interpro (Mitchell et al., 2015). In further details, from the number of residues in PAR-6::mcherry transgene, we estimated its radius to $r_{PAR-6} \simeq 2.9 \pm 0.8\ \text{nm}$ using (Wilkins et al., 1999), propagating error in the formula. This enabled us to obtain the viscosity using the diffusion coefficient for PAR-6::mcherry. Combining this estimate of viscosity and the

measured diffusion for DYCI-1::mcherry, the Stokes–Einstein–Sutherland equation gives $r_{DYCI-1} \simeq 17.0 \pm 7.3\ \text{nm}$ .This value corresponds to the one measured for human dynein dimer (Trokter et al., 2012), which displays a close estimated molecular weight (723 kD) compared to in *C. elegans* (675kD). We concluded that DYCI-1::mcherry very likely remains associated with the other members of the dynein complex in the cytoplasm.

Overall, the tube assay experiment together with DYCI-1 remaining associated in dynein complex suggest that DYCI-1::mcherry is a faithful reporter of dynein in its cortical pulling function during mitosis and likely also in its other roles in zygotic division.

1.2 CHARACTERIZING DYCI-1::MCHERRY DYNAMICS.

1.2.1 COUNTING MOLECULES BOUND TO THE MICROTUBULE PLUS-ENDS THROUGH TWO INDEPENDENT APPROACHES.

To estimate the number of DYCI-1::mcherry molecules at the growing end of the astral microtubules (plus-end), we used Fluorescence Correlation Spectroscopy (FCS). Because the intensity of fluorescence of the spots in DYCI-1::mcherry are weak, it is sometimes challenging to detect peaks reporting a dynein spot crossing the FCS volume (e.g. Fig. 3C). We needed a way to get the position of the spots independently from DYCI-1::mcherry spots ; indeed, because the faintest spots are likely not detected. To do so, we assumed a similar dynein binding kinetics to the spots between TH163 and doubly labeled DYCI-1::mcherry and EBP-2::GFP strain (see above). We put parameters (Fig. S1C) in eq. (S2) together with cytoplasmic concentration previously measured, 32 ± 11 molecules in FCS focal volume (N=8 embryos, 38 spots), and obtained 66 ± 5 dyneins (N=8 embryos, 43 spots) as an estimate of the number of particles in a spot.

We obtained however only an estimate and sought to gain confidence by reproducing the result through a secondary approach, based on comparing spots intensity to a reference after (Shivaraju et al., 2012). We used PAR-6::mcherry strain as reference and calibrated intensity, to be able to convert intensity into number of particles. We did so by comparing the background intensity in images of this strain (Fig. S10D) with the cytoplasmic concentration measured by FCS as described above (N=8 embryos, 16 spots, see §1.1.4). We then imaged PAR-6::mcherry and DYCI-1::mcherry in identical conditions (Fig. S10A-C) and fitted dynein spots intensity profile by a Gaussian with a background (b) to obtain the amplitude of the peak (A):

$$I = (A - b)\mathrm{e}^{-\frac{(x-\bar{x})^2}{2\sigma^2}} + b \qquad \text{(S3)}$$

where $\bar{x}$ is the spot position in the intensity profile and σ^2 its width (Fig S10E e.g.). We repeated this experiment in N=6 embryos, 20 spots and plotted a histogram of background-subtracted intensities (Fig. S10F), converted. The average intensity of dynein spots read 50 ± 13 particles, consistent with our previous estimate.

We also wished to compare this count of dynein per spot (microtubule plus-end) to the number of EBP-2::GFP. To measure it, we used the doubly labeled stain EBP2::GFP DYCI-1::mcherry. We measured the cytoplasmic concentration of EBP-2::GFP by FCS as explained above and got 82 ± 38 EBP-2::GFP in the 0.3 fl FCS volume. We also measured the intensity and used it to calibrate the relation between intensity and number of EBP-2::GFP. We then analyzed EBP-2::GFP spots at microtubule plus–ends crossing the FCS focal volume (Fig. 3C). Assuming that the basal level corresponded to the background previously measured, we estimated proportionally the number of particles for the peak. We found 185 ± 85 EBP-2::GFP per spot (N=8 embryos, 38 spots). This number is consistent with the number of DYCI-1::mcherry, putatively bound to EBP, found above.

1.2.2 COLOCALIZING DYCI-1::MCHERRY AND ASTRAL MICROTUBULES.

To quantify the colocalization of microtubule plus-end labeled by EBP-2::GFP and dynein, labeled by DYCI-1::mcherry (Fig. 3A, Movie S10), we tracked spots on both channels, then used a custom script. We considered instantaneous spatial coincidence of positions extracted from tracks, both for microtubule plus-ends and dyneins and with a tolerance of 4 pixels. We considered only tracks longer than 6 points (in the LSP) and 3 points (at the cortex) and displaying a directed motion. Because detection of dynein is more challenging than microtubule plus-end, we considered that a dynein track colocalized with microtubule plus-end when 75 % of its constituting points found a coincident point in microtubule plus-end channel.

In all cases, we wondered whether the high density of DYCI-1::mcherry spots might cause artefactual colocalization. Thus, for each colocalization experiment, we compared the result with the colocalization (using the same method) of a synthetic set of spots in identical number and randomly distributed in the image (Jaqaman et al., 2011). We found no significant colocalization with fabricated images in any experiment (Fig. S6B and Fig. 3B e.g.).

1.2.3 CHARACTERIZING DYNEIN UNBINDING DYNAMICS AT MICROTUBULE PLUS-END AND MODULATING MICROTUBULE GROWTH RATE.

We set to characterize the detachment of dynein from spots accumulated at microtubules plus-ends, in comparison to established dynamics of EBP-2/EB (Akhmanova and Steinmetz, 2015). To reword our question: how does the length of the "comet tail" of plus-end dynein accumulation vary when microtubule growth rate changes? To address this question, we plotted an intensity profile across dynein spots and, using an exponential fit, measured the length of the comet tail (see main text). To modulate microtubule growth rate, we used hypomorphic RNAi of genes altering microtubule dynamics: KLP-7/MCAK and CLIP-1/CLIP170 (Fig. S1A) (Srayko et al., 2005). Importantly, upon penetrant RNAi of these genes, we did not observe depletion of dynein from the plus-end (Fig. 5). In further details, we used 4 conditions, treating embryos by: (decreasing order of microtubule growth rate): *clip-1(RNAi)* during 48h (N=5 embryos, 3960 spots, 58 profiles); *clip-1(RNAi)*

during 24h (N=6 embryos, 2781 spots, 30 profiles); non treated embryos (N=8 embryos, 3000 spots, 30 profiles); and *klp-7(RNAi)* during 24h (N=6 embryos, 1067 spots, 30 profiles) (Fig. S1A). We observed a linear correlation between the comet length and microtubule growth rate (Fig. 3E and main text). We concluded that EBP-2/EB and DYCI-1 display the same unbinding dynamics at the microtubule plus-ends.

1.2.4 MEASUREMENT OF CORTICAL PULLING FORCES UPON DEPLETION OF KINESINS.

Kinesins are involved in budding yeast to create a secondary mechanism to target dynein at the cortex (Markus and Lee, 2011; Markus et al., 2009). More generally, kinesins are transporting dynein towards the cell periphery in other contexts (Hancock, 2014). We therefore tested the cortical forces generation upon RNAi silencing each of the genes encoding a kinesin motor domain, taken within the interpro corresponding family (Mitchell et al., 2015), in γTUB::GFP embryos. We excluded *vab-8* as it is not expressed in the embryo (Wolf et al., 1998). We observed a decrease in oscillation amplitudes, although non-significant, only for RNAi of klp-13, -18, -19, -20 (Fig. S9). Oscillations are indeed a read-out of cortical pulling forces (Pecreaux et al., 2006a). Klp-18 had previously been reported as playing no role in mitosis (Segbert et al., 2003). The others did not decrease dynein plus-end accumulation (Fig. 5B). We concluded that kinesin transport of dynein is likely not involved as secondary targeting mechanism to make EB proteins partially dispensable.

1.2.5 MEASURING DYNEIN RESIDENCY TIME AT THE CORTEX.

To measure the residency time of DYCI-1::mcherry at the cortex, we imaged the embryo during metaphase at the cortex plane, by moving the focus down until the embryo shape appeared diffuse. Next, the focus was moved up less than one micron recovering the embryo shape and set to this plane for imaging. The detected spots were tracked with the u-track package software and classified in two populations: direct and diffusive. We then computed the histogram of tracks duration for each population and averaged them over the embryos separately considering only tracks longer than 3 frames (600 ms). We estimated the residency time as the characteristic time $\mu = {}^{1}/_{\lambda}$ by fitting the averaged histograms with an exponential distribution (Fig. 2C):

$$1/\lambda * exp(-1/\lambda * t)$$

where t is the time.

1.2.6 ESTIMATING THE RATE OF DYNEIN REACHING THE CORTEX BY 3D DIFFUSION.

Interestingly, using (Von Smoluchowski, 1917), we can estimate the rate of dynein reaching the cortex by 3D diffusion for a half–spheroidal embryo $r \simeq 30\ \text{dynein}/\text{s}$, in steady state regime (assuming recycling to the cell center performs at a non-limiting rate). Equation reads $r = 2\pi DRc_0$ with $D = 2.6\,\mu m^2/s$ the diffusion coefficient (see above), $R = 17.0\,nm$ the hydrodynamics radius of dynein dimer (Trokter et al., 2012) and

$c_0 = 3.2 \times 10^{18}$ dynein/m^3 the concentration estimated above. It appears in the good order of magnitude although a bit small in comparison to 20 to 200 expected from the 10 to 100 active force generators per half cortex (Grill et al., 2003) that stay ~0.5s (this work) and (Pecreaux et al., 2006a).

1.3 IMAGE PROCESSING PIPELINE TO CHARACTERIZE DYNEIN DYNAMICS

1.3.1 PREPROCESSING OF THE IMAGES

Since dynein spots are very weak, we denoised the images to filter out the contribution of cytoplasmic fraction and increase the signal-to-noise ratio. Such a denoising usually relies on the assumption that the noise is non-correlated in space and time and follows a Gaussian or Poisson distribution. We reasoned that since we have a threshold in the count of dyneins per spot, under-threshold spots could contribute to the background and create space and time correlation. We therefore opted for the CANLDE filtering/denoising (Coupe et al., 2012) (Fig. S4AB). We used parameters that allowed a proper view of the fine structures and enabled us to distinguish close individual spots: smoothing parameter beta was 0.05, patch radius 1 (voxel of 3x3x3) and search volume radius 3. Fast processing of the dark background was used since normal processing did not produce further improvement. Processed images were then submitted to spot enhancer (Sage et al., 2005) using a Laplacian of Gaussian filter with standard deviation σ=1.25 (Fig. S4C).

1.3.2 AUTOMATED TRACKING OF DYCI-1::MCHERRY FLUORESCENT SPOTS.

Because multiple tracks are present and could cross each other, we sought an algorithm with robust linking. We opted for u-track (Jaqaman et al., 2008) with parameters reproduced in supplementary table S1 below. We validated these parameters by analyzing fabricated images of known dynamics (see simulation section below) and found good colocalization between prescribed tracks in simulation and recovered ones (Fig. S5F). We obtained the density of tracks by dividing by the duration of the acquisition and the area of the embryo. When considering LSP, we excluded the spindle, obtained by a semi-supervised segmentation. Because we were conservative in parameterizing u-track algorithm, it is possible that some long tracks were broken into pieces. Furthermore, the plus-end of the microtubule is only transiently in the focal plane when imaging in LSP.

Supplementary Table S1: Parameters used for tracking with software package u-track.

Detection	
Gaussian standard deviation	Iterate to estimate Gaussian standard deviation. Maximum number of iterations 10

Rolling window time-averaging	3
Iterative Gaussian mixture-model fitting	No
Tracking	
Maximum gap to close	Cytosol (8), cortex (3)
Merge split	0
Minimum length of track segments from first step	Cytosol (3), cortex (6)
Cost function frame-to frame linking	
Flag for linear motion	1
Allow instantaneous direction reversal	Cytosol (0), cortex (1)
Search radius lower limit	2
Search radius upper limit	5
Standard deviation multiplication factor	1
Nearest neighbor distance calculation	1
Number of frames for Nearest neighbor distance calculation	9
Cost function close gaps	
Flag for linear motion	1
Search radius lower limit	2
Search radius upper limit	5
Standard deviation multiplication factor	3
Nearest neighbor distance calculation	
Number of frames for nearest neighbor distance calculation	9
Penalty for increasing gap length	1.5
Maximum angle between linear tracks segments	30

1.3.3 CLASSIFICATION OF THE TRACKS

To characterize the dynamics of the spots, we classified the tracks according to 3 features: (1) the directionality, (2) the sense (centrifugal/centripetal) and finally (3) the model of motion between flow and diffusion (see a typical velocity map in Fig. S8).

1. Classification of tracks according to their asymmetry.

Visual inspection of tracks (Fig. 2AB) suggested that some might be directed. We therefore classified them between anisotropic (directed) or isotropic (diffusive-like) using the asymmetry of the trajectories and following the method proposed in (Huet et al., 2006; Jaqaman et al., 2008). Tracks shorter than 5 frames (in cytoplasm/LSP) and 3 frames (at the cortex) were not considered for this analysis. We chose the parameter alpha (the threshold for classification) to 0.1 (90 percentile).

2. Classification of linear trajectories according to the sense.

We expected different molecular mechanisms for directed motion of tracks of different senses. We therefore classified the directed trajectories according to their motion direction *toward the periphery* or *toward the center*: We first segmented the embryo contour using a supervised segmentation and, for each track, computed the Euclidean distance of each point of the track to the embryo contour curve forming a vector of distance to cortex of same length as the track. The difference between adjacent elements of this vector reported whether a step in the track brought the spot closer to or further from the cortex. Eventually, for each track, we computed the probability Θ of moving towards the cortex as the ratio of the number of steps getting the spot closer to the cortex to the total number of steps in this track. Tracks with Θ above 0.7 were classified as moving towards the cell cortex. Similar ratio and threshold were used, *mutatis mutandis*, to classify tracks moving towards the centrosome. Doing so, we excluded the few tracks that showed no clear sense from further treatment. Exemplar results are reproduced in Fig. 2ABE.

3. Classification according to the model of motion.

To characterize the motion of the spots in each of the directionality and sense class, we set to estimate the probability for the tracks in a given class to display classic motion as flow or various kinds of diffusion. We used Bayesian classifier in the implementation of Monnier and co-authors (Monnier et al., 2012), later referred as BCA. We tested three alternative models, normal diffusion (D), flow (V) and flow mixed with diffusion (DV) in LSP and diffusive (D), anomalous-diffusion (AD) and confined diffusion (CD) at the cortex (Saxton, 1994). To do so, we computed the conditional probability of each model knowing the data using mean square displacement (MSD) with a given time lag (Fig. S12). We repeated the computation of probability over a range of time lag, 6-16 frames in LSP and 3-16 frames at the cortex, and averaged the results. Eventually, to estimate the speed using flow or mixture flow-diffusion models, we considered the time lag resulting into the highest conditional probability and retrieved the parameters of fitted model, (V) or (DV) (Monnier et al., 2012). Exemplar results are reproduced in Fig. 2FG.

1.3.4 ANALYSING SIMULATED MICROSCOPY IMAGES TO VALIDATE THE IMAGE PROCESSING AND DATA ANALYSIS PIPELINE.

To ensure that our image processing pipeline gives a faithful characterizing of spots dynamics, we fabricated synthetic fluorescent images, which mimic our experimental data (Costantino et al., 2005) (Fig. S5A). In further details, we simulated stochastic trajectories of particles, either in pure diffusion with $x_{i,j}(t+1) = x_{i,j}(t) + \xi\sqrt{2Dt}$ (Movie S7) or adding a flow on top of it with $x_{i,j}\ (t) = x_{i,j}(t) + \xi\sqrt{2Dt} + v_{i,j}t$ (Movie S8), where $x_{i,j}(t)$ represents the coordinate in two dimensions at time t, ξ is a random number , D is the diffusion coefficient and $v_{i,j}$ is the flow speed. The duration of the tracks (length) was sampled from an exponential distribution. The intensity was set similar to experimental ones and encoded by the quantum yield parameter (Qyield). We then plotted the instantaneous positions and applied a Gaussian filter to mimic the effect of the point-spread function in fluorescence microscopy. We then added two flavors of noise: first, we mimicked the background noise by adding at each pixel a sampling of a Gaussian distribution normalized to **ε,** with formula reading $A_{noisy} = A + \epsilon M$ and corresponding to a signal to noise ratio $Max(A)/_{\epsilon}$; second, we mimicked the fluorescent background by superimposing a large number of fast diffusing particles to the noisy image. This simulation provided a realistic scenario to test the image processing and data analysis pipeline. Details of the parameters used for simulation can be found in table S2.

Supplementary Table S2: Parameters of simulated images of dynein dynamics.

Image size	250x250 pixels
Duration	100 frames (20s)
Density of particles (tracks)	(0.15 particles/μm^2)
Density of fast diffusing background particles	900 particles/μm^2
Qyield	0.42 (mcherry)
Pixel size	0.130 nm
Sampling rate	0.2 s
PSF Type	Gaussian
PSF size	0.3 μm
Bits	12
Diffusion coefficient	0.002 μm^2/s
Flow Speed (x and y coordinate)	0.4 μm/s
Background noise standard deviation σ	0.1,0.3,0.5,0.7
Mean tracks lifetime (mean of exponential distribution)	10
Diffusion coefficient of background particles	2.1 μm^2/s
Mean tracks lifetime (mean of exponential distribution) for background particles	2 s

We then processed these fabricated images as the real ones (Fig. S5BC) and analyzed them. The comparison of the result recovered by our analysis pipeline with the values set in the simulation for physical parameters (ground-truth) suggests that analysis pipeline performed faithfully in the signal-to-noise ratio (SNR) range, where we laid experimentally (Fig. S5D-G, main text).

2. MATERIALS AND METHODS

2.1 CULTURING C. ELEGANS

C. elegans were cultured as described in (Brenner, 1974) and dissected to obtain embryos. All strains containing DYCI-1::mcherry were maintained at 25ºC while functional experiments (anaphase oscillations) investigating the role of CLIP170, EB homologs and kinesins were performed at 18ºC, except for clip-1(gk470) at 23ºC, and corresponding strain cultured at the same temperature.

2.2 C. ELEGANS STRAINS USED

The Bristol strain N2 was used as the standard wild-type strain (Brenner, 1974). Following fluorescent strains were used: TH163 (DYCI-1::mCherry) (Sarov et al., 2006); TH27 (GFP::TBG-1) (Oegema et al., 2001); TH65 (YFP::TBA-2) (Kozlowski et al., 2007); TH66 (GFP::EBP-2) (Srayko et al., 2005); DE74 (GFP::PLCδ1-PH) (Johnston et al., 2010); TH110 (mcherry::PAR-6) (Schonegg et al., 2007). The following multi-labeled combinations were generated through standard genetics crosses: JEP2 (DYCI-1::mCherry/YFP::TBA-2); JEP12 (DYCI-1::mCherry/ GFP::EBP-2); JEP20 (DYCI-1::mCherry/ GFP::PLCδ1-PH). JEP27 and JEP32, carrying GFP::TBG-1 transgene and *ebp-2(gk756)* or *clip-1(gk470)* mutation, respectively, were obtained by crossing TH27 with VC1614 or VC1071 (Consortium, 2012). The strain carrying the *dyci-1(tm4732)* lethal mutation was provided by the Mitani Lab, through the National Bio-resource Project. JEP30 and JEP40 strains, homozygous for *dyci-1(tm4732)*, were obtained by double crossing JEP23 or TH163 respectively, with JEP9. The transgenes encoding the GFP, YFP or mcherry fusion proteins in all constructs but DYCI-1::mcherry were under the control of the pie-1 promoter.

2.3 GENE SILENCING BY RNA INTERFERENCE

Except otherwise stated, embryonic RNAi were performed by feeding using the Ahringer-Source BioScience library (Fire et al., 1998; Kamath and Ahringer, 2003) and using clones ordered from Source BioScience. Clones for ebp-1/3 and klp-18 were made in the lab: a region from the target gene (see table S3) was amplified using N2 genomic DNA, cloned into the RNAi feeding vector L4440 and transformed into HT115 bacteria. For ebp-1, one region corresponding to exon 2 and 3 after splicing was amplified using four long primers and fused by PCR amplification before cloning into L4440. Primers used to amplify are listed in the table:

Supplementary Table S3: Primers used in this study.

target	Primer forward	Primer reverse
ebp -1/3	5' ACCGGGAGTCGATATGGC 3'	5' TCAACATTTCCAATCGATTCATT 3'
ebp-1	5' TCGTCTTGAATTGGATTGG CTTTCCAACTGGAAACTAGTG CAGACTACGTGGAAGAATTT 3' 5' GATTAAGGGAAAATTTCAG GACAACTTTGAATTCTTGCAA TGGTTCAAGAAATTGTTCGAT GCTAACTATGATGGACATGA GTATGA 3'	5' TTGTCCTGAAATTTTCCCTTAA TCAATTTATCAACAGGAATCACTT TCTCGACACCCAAATTCTTCCACG TAGTCTGCAC 3' 5' CATTACGTGCTTGCATTGGATC ATACTCATGTCCATCATAGTTAG C 3'
klp-18	5' ACGGAATTCGCATCACAGT T 3'	5' CAATCTGTTCGTTTTCTGATCC 3'

For *ebp-1* and *ebp-1/3* RNAi treatments, we observed 40-60 % reduction of the number of transcript by Q-RT-PCR without affecting mRNA level of *ebp-2*. Total RNA was extracted from around 20 worms using Direct-Zol RNA Microprep Kit from Zymo Research. cDNA was produced using Protoscript II First Strand cDNA Synthesis Kit from New England Biolabs. For Q-PCR, Power SYBR Green PCR master mix was used with 7900HT Fast Real-Time PCR System from Applied Biosystems.

To take into account the variability of the expression of DYCI-1::mcherry in the randomly integrated strain, each RNAi experiment was compared or normalized to non-treated embryos imaged on the same day (e.g. Fig. 4AB, 5, 6BCD).

Except otherwise stated, RNAi were partial: observation was performed 23-25h after plating the worms. In particular and to avoid too strong or unrelated phenotypes, we used the following duration of treatment when observing randomly integrated DYCI-1::mcherry strain (TH163): *lin-5(RNAi)* 17h, *gpr-1/2(RNAi) 48h*, *lis-1(RNAi)* 18h, *klp-3(RNAi)* 18h, *klp-7(RNAi)* 18h, *dnc-1(RNAi)* 16h, *ebp-2(RNAi)* 20h. When investigating oscillations using γ TUB::GFP (TH27), kinesins where observed after 24h of treatment, dynein subunit *dyci-1(RNAi)* after 16h and *dli-1(RNAi)* after 24h

2.4 LIVE IMAGING

Embryos were dissected in M9 buffer and mounted on a 2% w/v agarose, 0.6 % w/v NaCl and 4 % w/v sucrose pads. We imaged *C. elegans* one–cell embryo during metaphase and anaphase. Dynein/EBP-2 tracking was performed on a LEICA DMI6000 / Yokogawa CSU-X1 M1 spinning disc microscope, using HCX Plan Apo. 100x/NA 1.4 Oil.

Illumination was performed by a white light Fianium laser conveniently filtered around 488 nm and 561 nm by an homemade setup (patent pending (Roul et al., 2015)). Images were acquired with a 200 ms exposure time (5 Hz) using a Roper instrument evolve camera and the Metamorph software (Universal imaging Corp.) without binning. We kept the embryos at 24 °C during the experiments. To image embryos at LSP we moved the focus typically between 3 and 5 µm below the spindle plane (Fig. S1D). Typically, LSP is 10-11 µm above the cortex plane. Double-labeled embryos were imaged at 2.5Hz.

To track centrosome, imaging was performed in the mid-plane using a Zeiss AxioImager upright microscope modified for long-term time-lapse. First, an extra anti-heat filter was added on the mercury lamp light path. Second, to decrease the bleaching and obtain optimal excitation, we used an enhanced transmission 12 nm band-pass excitation filter centered on 485 nm (AHF analysentechnik, Tübingen, Germany). We used a 100x/NA 1.45 Oil plan-Apo objectives. Images were acquired with an Andor Ixon3 EMCCD 512x512 camera at 33 frames per second and using the Solis software. Images were archived using Omero software.

2.5 FCS AND FCCS MEASUREMENTS

We performed fluorescent correlation spectroscopy experiments with a leica SP8 microscope equipped with a continuous laser and water immersion 60x/1.2NA plan-Apo. objective. The GFP was excited either with 488 nm line laser or 488 nm pulsed Ar laser; mCherry was excited with 561 nm laser diode. We measured at least 3 points per embryos during 30 s each time. We kept the temperature at 24 °C. Experimental autocorrelation functions were analyzed using the Picoquant software package and fitted to the expression (S1). Cross-correlation between EBP-2::GFP and DYCI-1::mcherry was analyzed as described in (Padilla-Parra et al., 2011) using pulsed laser illumination.

2.6 IMAGE PROCESSING

The Standard Deviation Maps (SDM) were generated with "Z Project" plugin of Fiji with type "standard deviation" over 6 s of the time-lapse image sequence (Cai et al., 2007; Rostampour et al., 1988).

Tracking of centrosomes and analysis of trajectories were performed by a custom tracking software based on [31] and developed using Matlab (The MathWorks). Tracking of -20ºC methanol-fixed γTUB::GFP embryos indicated an accuracy of 10 nm. Embryo orientation and center were obtained by cross-correlation of embryo background cytoplasmic fluorescence with an artificial binary image mimicking an embryo or by contour detection of the cytoplasmic membrane using background fluorescence of cytoplasmic γTUB::GFP with help of an active contour algorithm (Pecreaux et al., 2006b). Results were averaged over all *replica* for each condition.

2.7 STATISTICS

Center valued displayed are means except otherwise stated. Averaged values were compared using two-sided Student t-test with Welch-Satterwaithe correction for unequal variance except otherwise stated. For sake of simplicity, we encoded confidence level using

stars: ♦ meaning $p<0.1$, * meaning $p\leq0.05$, ** $p\leq0.01$, *** $p\leq0.001$, **** $p\leq0.0001$ and n.s. (for non-significant) meaning $p> 0.1$. n.s. indication might be omitted for sake of clarity. We abbreviated standard deviation by S.D., standard error by s.e. and standard error of the mean by s.e.m.

2.8 CODE AND DATA AVAILABILITY

The computer codes generated during the current study are available from the corresponding author on reasonable request. The datasets generated and analyzed during the current study are available from the corresponding author on reasonable request.

3. REFERENCES

.

Akhmanova, A., and Steinmetz, M.O. (2015). Control of microtubule organization and dynamics: two ends in the limelight. Nat Rev Mol Cell Biol.

Boulin, T., and Bessereau, J.L. (2007). Mos1-mediated insertional mutagenesis in Caenorhabditis elegans. Nat Protoc *2*, 1276-1287.

Brenner, S. (1974). The genetics of Caenorhabditis elegans. Genetics *77*, 71-94.

Cai, D., Verhey, K.J., and Meyhofer, E. (2007). Tracking single Kinesin molecules in the cytoplasm of mammalian cells. Biophys J *92*, 4137-4144.

Consortium, C.e.D.M. (2012). large-scale screening for targeted knockouts in the Caenorhabditis elegans genome. G3 *2*, 1415-1425.

Costantino, S., Comeau, J.W., Kolin, D.L., and Wiseman, P.W. (2005). Accuracy and dynamic range of spatial image correlation and cross-correlation spectroscopy. Biophys J *89*, 1251-1260.

Coupe, P., Munz, M., Manjon, J.V., Ruthazer, E.S., and Collins, D.L. (2012). A CANDLE for a deeper in vivo insight. Med Image Anal *16*, 849-864.

Dernyi, I., Jlicher, F., and Prost, J. (2002). Formation and Interaction of Membrane Tubes. Physical Review Letters *88*, 238101.

Fire, A., Xu, S., Montgomery, M.K., Kostas, S.A., Driver, S.E., and Mello, C.C. (1998). Potent and specific genetic interference by double-stranded RNA in Caenorhabditis elegans. Nature *391*, 806-811.

Garrard, S.M., Capaldo, C.T., Gao, L., Rosen, M.K., Macara, I.G., and Tomchick, D.R. (2003). Structure of Cdc42 in a complex with the GTPase-binding domain of the cell polarity protein, Par6. EMBO J *22*, 1125-1133.

Grill, S.W., Howard, J., Schaffer, E., Stelzer, E.H., and Hyman, A.A. (2003). The distribution of active force generators controls mitotic spindle position. Science *301*, 518-521.

Hancock, W.O. (2014). Bidirectional cargo transport: moving beyond tug of war. Nat Rev Mol Cell Biol *15*, 615-628.

Hirano, Y., Yoshinaga, S., Takeya, R., Suzuki, N.N., Horiuchi, M., Kohjima, M., Sumimoto, H., and Inagaki, F. (2005). Structure of a cell polarity regulator, a complex between atypical PKC and Par6 PB1 domains. J Biol Chem *280*, 9653-9661.

Howard, J. (2001). Mechanics of motor proteins and the cytoskeleton (Sunderland, Mass.: Sinauer Associates, Publishers).

Huet, S., Karatekin, E., Tran, V.S., Fanget, I., Cribier, S., and Henry, J.P. (2006). Analysis of transient behavior in complex trajectories: application to secretory vesicle dynamics. Biophys J *91*, 3542-3559.

Jaqaman, K., Kuwata, H., Touret, N., Collins, R., Trimble, W.S., Danuser, G., and Grinstein, S. (2011). Cytoskeletal control of CD36 diffusion promotes its receptor and signaling function. Cell *146*, 593-606.

Jaqaman, K., Loerke, D., Mettlen, M., Kuwata, H., Grinstein, S., Schmid, S.L., and Danuser, G. (2008). Robust single-particle tracking in live-cell time-lapse sequences. Nature methods *5*, 695-702.

Johnston, W.L., Krizus, A., and Dennis, J.W. (2010). Eggshell chitin and chitin-interacting proteins prevent polyspermy in C. elegans. Curr Biol *20*, 1932-1937.

Kamath, R.S., and Ahringer, J. (2003). Genome-wide RNAi screening in Caenorhabditis elegans. Methods *30*, 313-321.

Kamath, R.S., Fraser, A.G., Dong, Y., Poulin, G., Durbin, R., Gotta, M., Kanapin, A., Le Bot, N., Moreno, S., Sohrmann, M.*, et al.* (2003). Systematic functional analysis of the Caenorhabditis elegans genome using RNAi. Nature *421*, 231-237.

Kozlowski, C., Srayko, M., and Nedelec, F. (2007). Cortical microtubule contacts position the spindle in C. elegans embryos. Cell *129*, 499-510.

Leduc, C., Campas, O., Zeldovich, K.B., Roux, A., Jolimaitre, P., Bourel-Bonnet, L., Goud, B., Joanny, J.F., Bassereau, P., and Prost, J. (2004). Cooperative extraction of membrane nanotubes by molecular motors. Proc Natl Acad Sci U S A *101*, 17096-17101.

Markus, S.M., and Lee, W.L. (2011). Regulated offloading of cytoplasmic dynein from microtubule plus ends to the cortex. Dev Cell *20*, 639-651.

Markus, S.M., Punch, J.J., and Lee, W.L. (2009). Motor- and tail-dependent targeting of dynein to microtubule plus ends and the cell cortex. Curr Biol *19*, 196-205.

Mi, H., Dong, Q., Muruganujan, A., Gaudet, P., Lewis, S., and Thomas, P.D. (2010). PANTHER version 7: improved phylogenetic trees, orthologs and collaboration with the Gene Ontology Consortium. Nucleic Acids Res *38*, D204-210.

Mi, H., Muruganujan, A., Casagrande, J.T., and Thomas, P.D. (2013). Large-scale gene function analysis with the PANTHER classification system. Nat Protocols *8*, 1551-1566.

Mitchell, A., Chang, H.Y., Daugherty, L., Fraser, M., Hunter, S., Lopez, R., McAnulla, C., McMenamin, C., Nuka, G., Pesseat, S., *et al.* (2015). The InterPro protein families database: the classification resource after 15 years. Nucleic Acids Res *43*, D213-221.

Monnier, N., Guo, S.M., Mori, M., He, J., Lenart, P., and Bathe, M. (2012). Bayesian approach to MSD-based analysis of particle motion in live cells. Biophys J *103*, 616-626.

Nguyen-Ngoc, T., Afshar, K., and Gonczy, P. (2007). Coupling of cortical dynein and G alpha proteins mediates spindle positioning in Caenorhabditis elegans. Nat Cell Biol *9*, 1294-1302.

Oegema, K., Desai, A., Rybina, S., Kirkham, M., and Hyman, A.A. (2001). Functional analysis of kinetochore assembly in Caenorhabditis elegans. The Journal of Cell Biology *153*, 1209-1226.

Padilla-Parra, S., Auduge, N., Coppey-Moisan, M., and Tramier, M. (2011). Dual-color fluorescence lifetime correlation spectroscopy to quantify protein-protein interactions in live cell. Microsc Res Tech *74*, 788-793.

Pecreaux, J., Roper, J.C., Kruse, K., Julicher, F., Hyman, A.A., Grill, S.W., and Howard, J. (2006a). Spindle oscillations during asymmetric cell division require a threshold number of active cortical force generators. Curr Biol *16*, 2111-2122.

Pecreaux, J., Zimmer, C., and Olivo-Marin, J.C. (2006b). Biophysical active contours for cell tracking I: Tension and bending. In 2006 Ieee International Conference on Image Processing, Icip 2006, Proceedings (October 8-11 2006, Atlanta, GA, USA), pp. 1949-1952.

Redemann, S., Pecreaux, J., Goehring, N.W., Khairy, K., Stelzer, E.H., Hyman, A.A., and Howard, J. (2010). Membrane invaginations reveal cortical sites that pull on mitotic spindles in one-cell C. elegans embryos. PLoS One *5*, e12301.

Robert, V., and Bessereau, J.L. (2007). Targeted engineering of the Caenorhabditis elegans genome following Mos1-triggered chromosomal breaks. Embo J *26*, 170-183.

Rostampour, A.R., Reeves, A.P., and Mitchell, O.R. (1988). Use of temporal variance for moving object extraction. Paper presented at: Computers and Communications, 1988 Conference Proceedings, Seventh Annual International Phoenix Conference on.

Roul, J., Pecreaux, J., and Tramier, M. (2015). Procédé de pilotage multi-‒ ‑ modules fonctionnels incluant un dispositif d’ imagerie multi-‒-longueur d’ onde, et système de pilotage correspondant, L.H. Office européen des brevets, ed.

Sage, D., Neumann, F.R., Hediger, F., Gasser, S.M., and Unser, M. (2005). Automatic tracking of individual fluorescence particles: application to the study of chromosome dynamics. IEEE Trans Image Process *14*, 1372-1383.

Sarov, M., Murray, J.I., Schanze, K., Pozniakovski, A., Niu, W., Angermann, K., Hasse, S., Rupprecht, M., Vinis, E., Tinney, M., *et al.* (2012). A genome-scale resource for in vivo tag-based protein function exploration in C. elegans. Cell *150*, 855-866.

Sarov, M., Schneider, S., Pozniakovski, A., Roguev, A., Ernst, S., Zhang, Y., Hyman, A.A., and Stewart, A.F. (2006). A recombineering pipeline for functional genomics applied to Caenorhabditis elegans. Nat Methods *3*, 839-844.

Saxton, M.J. (1994). Single-particle tracking: models of directed transport. Biophys J *67*, 2110-2119.

Schonegg, S., Constantinescu, A.T., Hoege, C., and Hyman, A.A. (2007). The Rho GTPase-activating proteins RGA-3 and RGA-4 are required to set the initial size of PAR domains in Caenorhabditis elegans one-cell embryos. Proc Natl Acad Sci U S A *104*, 14976-14981.

Segbert, C., Barkus, R., Powers, J., Strome, S., Saxton, W.M., and Bossinger, O. (2003). KLP-18, a Klp2 kinesin, is required for assembly of acentrosomal meiotic spindles in Caenorhabditis elegans. Mol Biol Cell *14*, 4458-4469.

Shivaraju, M., Unruh, J.R., Slaughter, B.D., Mattingly, M., Berman, J., and Gerton, J.L. (2012). Cell-cycle-coupled structural oscillation of centromeric nucleosomes in yeast. Cell *150*, 304-316.

Sonnichsen, B., Koski, L.B., Walsh, A., Marschall, P., Neumann, B., Brehm, M., Alleaume, A.M., Artelt, J., Bettencourt, P., Cassin, E.*, et al.* (2005). Full-genome RNAi profiling of early embryogenesis in Caenorhabditis elegans. Nature *434*, 462-469.

Srayko, M., Kaya, A., Stamford, J., and Hyman, A.A. (2005). Identification and characterization of factors required for microtubule growth and nucleation in the early C. elegans embryo. Dev Cell *9*, 223-236.

Trokter, M., Mucke, N., and Surrey, T. (2012). Reconstitution of the human cytoplasmic dynein complex. Proc Natl Acad Sci U S A *109*, 20895-20900.

Von Smoluchowski, M. (1917). Versuch einer mathematischen Theorie der Koagulationskinetik kolloidaler Lösungen. Zeitschrift für physikalische Chemie *92*, 129-168.

Widengren, J., Rigler, R., and Mets, U. (1994). Triplet-state monitoring by fluorescence correlation spectroscopy. Journal of fluorescence *4*, 255-258.

Wilkins, D.K., Grimshaw, S.B., Receveur, V., Dobson, C.M., Jones, J.A., and Smith, L.J. (1999). Hydrodynamic radii of native and denatured proteins measured by pulse field gradient NMR techniques. Biochemistry *38*, 16424-16431.

Wolf, F.W., Hung, M.S., Wightman, B., Way, J., and Garriga, G. (1998). vab-8 is a key regulator of posteriorly directed migrations in C. elegans and encodes a novel protein with kinesin motor similarity. Neuron *20*, 655-666.